



Nebular Emission Line Ratios in $z \simeq 2\text{--}3$ Star-forming Galaxies with KBSS-MOSFIRE: Exploring the Impact of Ionization, Excitation, and Nitrogen-to-Oxygen Ratio*

Allison L. Strom¹, Charles C. Steidel¹, Gwen C. Rudie², Ryan F. Trainor³, Max Pettini⁴, and Naveen A. Reddy⁵¹ Cahill Center for Astronomy and Astrophysics, California Institute of Technology, MS 249-17, Pasadena, CA 91125, USA; astrom@astro.caltech.edu² Carnegie Observatories, 813 Santa Barbara Street, Pasadena, CA 91101, USA³ Department of Astronomy, University of California, Berkeley, New Campbell Hall, Berkeley, CA 94720, USA⁴ Institute of Astronomy, Madingley Road, Cambridge CB3 0HA, UK⁵ Department of Physics and Astronomy, University of California, Riverside, 900 University Avenue, Riverside, CA 92521, USA

Received 2016 August 2; revised 2017 January 12; accepted 2017 January 16; published 2017 February 17

Abstract

We present a detailed study of the rest-optical (3600–7000 Å) nebular spectra of ~ 380 star-forming galaxies at $z \simeq 2\text{--}3$, obtained with Keck/Multi-object Spectrometer for Infrared Exploration (MOSFIRE) as part of the Keck Baryonic Structure Survey (KBSS). The KBSS-MOSFIRE sample is representative of star-forming galaxies at these redshifts, with stellar masses $M_* = 10^9\text{--}10^{11.5} M_\odot$ and star formation rates $\text{SFR} = 3\text{--}1000 M_\odot \text{ yr}^{-1}$. We focus on robust measurements of many strong diagnostic emission lines for individual galaxies: [O II] $\lambda\lambda 3727, 3729$, [Ne III] $\lambda 3869$, H β , [O III] $\lambda\lambda 4960, 5008$, [N II] $\lambda\lambda 6549, 6585$, H α , and [S II] $\lambda\lambda 6718, 6732$. Comparisons with observations of typical local galaxies from the Sloan Digital Sky Survey and between subsamples of KBSS-MOSFIRE show that high-redshift galaxies exhibit a number of significant differences in addition to the well-known offset in $\log([\text{O III}]\lambda 5008/\text{H}\beta)$ and $\log([\text{N II}]\lambda 6585/\text{H}\alpha)$. We argue that the primary difference between H II regions in $z \sim 2.3$ galaxies and those at $z \sim 0$ is an enhancement in the degree of nebular excitation, as measured by [O III]/H β and $R23 \equiv \log([\text{O III}]\lambda\lambda 4960, 5008 + [\text{O II}]\lambda\lambda 3727, 3729)/\text{H}\beta$. At the same time, KBSS-MOSFIRE galaxies are ~ 10 times more massive than $z \sim 0$ galaxies with similar ionizing spectra and have higher N/O (likely accompanied by higher O/H) at fixed excitation. These results indicate the presence of harder ionizing radiation fields at fixed N/O and O/H relative to typical $z \sim 0$ galaxies, consistent with Fe-poor stellar population models that include massive binaries, and highlight a population of massive, high-specific star formation rate galaxies at high redshift with systematically different star formation histories than galaxies of similar stellar mass today.

Key words: cosmology: observations – galaxies: evolution – galaxies: high-redshift – galaxies: ISM – H II regions – ISM: abundances

1. Introduction

The strong emission lines of elements such as hydrogen, oxygen, and nitrogen observed in the rest-optical (3600–7000 Å) spectra of galaxies come primarily from the H II regions surrounding massive O and B stars. Thus attempts to characterize this emission ultimately reveal information regarding the properties of both the massive stars and the ionized gas immediately surrounding them. Furthermore, we know from studies of individual H II regions in the Milky Way and nearby galaxies that changes in the nebular spectrum are tightly correlated with one another, manifesting the underlying correlations between the physical properties of the ionized regions—including electron density, electron temperature, gas chemistry, and ionization parameter—that determine the strength of emission lines.

Studies conducted using integrated-light spectra of large samples of nearby galaxies, such as the Sloan Digital Sky Survey (SDSS, York et al. 2000), reveal similar behavior in galaxies spanning a wide range in stellar mass and star formation rate (SFR), with star-forming galaxies occupying a tight locus in many parameter spaces. For example, low- z star-forming galaxies form a relatively narrow sequence in the log

([O III] $\lambda 5008/\text{H}\beta$) versus $\log([\text{N II}]\lambda 6585/\text{H}\alpha)$ plane (hereafter the N2-BPT diagram), extending from high [O III]/H β and low [N II]/H α to low [O III]/H β and high [N II]/H α as gas-phase metallicity increases and the level of ionization decreases. The position of objects in the N2-BPT plane can therefore be used as a tool for distinguishing galaxies powered by young stars from galaxies with significantly harder ionizing radiation fields (such as those produced by active galactic nuclei, or AGN). The very hard ionizing spectrum of AGN produces enhanced collisional line emission in an extended partially ionized region, resulting in a diffuse “plume” that extends to both high [O III]/H β and high [N II]/H α in the N2-BPT plane.

The use of line ratios to distinguish between sources of ionizing radiation was first proposed by Baldwin et al. (1981), but Veilleux & Osterbrock (1987) introduced the version of the N2-BPT diagram commonly used today (along with two other diagnostic diagrams using [S II] $\lambda\lambda 6718, 6733/\text{H}\alpha$ and [O I] $\lambda 6300/\text{H}\alpha$ instead of [N II] $\lambda 6585/\text{H}\alpha$). Kewley et al. (2001) and Kauffmann et al. (2003) separately provided classification curves that are now frequently used to separate $z \sim 0$ star-forming galaxies from AGN in the N2-BPT plane; the former relied on predictions from photoionization models, but the latter specifically considered the importance of correlations between the physical conditions in star-forming galaxies, particularly between metallicity and ionization parameter.

* The data presented in this paper were obtained at the W.M. Keck Observatory, which is operated as a scientific partnership among the California Institute of Technology, the University of California, and the National Aeronautics and Space Administration. The observatory was made possible by the generous financial support of the W.M. Keck Foundation.

Advances in our knowledge of the conditions (and the important correlations between them) in galaxies at earlier epochs—specifically $z \simeq 2\text{--}3$, when both cosmic star formation (e.g., Madau et al. 1996; Hopkins & Beacom 2006; Reddy et al. 2008; Madau & Dickinson 2014) and supermassive black hole accretion reached their peak values (Richards et al. 2006)—have been slower to arrive, due in large part to limitations in the sensitivity and multiplexing capabilities of near-infrared spectrographs on 8–10 m class telescopes. Still, early observations of small samples of high-redshift galaxies (e.g., Shapley et al. 2005; Erb et al. 2006a; Liu et al. 2008) suggested that the situation at high- z might be radically different, with galaxies exhibiting lower gas-phase oxygen abundance at fixed stellar mass and nebular line ratios inconsistent with observations of the majority of local galaxies. Since the commissioning of efficient multi-object near-infrared spectrographs like the K band Multi-object Spectrograph on the VLT (KMOS, Sharples et al. 2013) and the Multi-object Spectrometer for Infrared Exploration on the Keck I telescope (MOSFIRE, McLean et al. 2012), the number of $z \simeq 2\text{--}3$ galaxies with high-quality rest-optical spectra has increased dramatically (Steidel et al. 2014; Kriek et al. 2015; Wisnioski et al. 2015). The results from galaxy surveys using these instruments have confirmed that while high-redshift star-forming galaxies also occupy a relatively tight locus in the N2-BPT diagnostic diagram, they show a clear offset toward higher $[\text{O III}]\lambda 5008/\text{H}\beta$ at a given $[\text{N II}]\lambda 6585/\text{H}\alpha$ compared to their low-redshift counterparts (Masters et al. 2014; Steidel et al. 2014; Shapley et al. 2015).

Systematic differences between typical star-forming galaxies in the local universe and those present during the peak epoch of galaxy growth are not surprising—on average, $z \sim 2$ galaxies have higher SFRs at fixed mass by at least a factor of 10 and cold gas masses higher by at least a factor of ~ 5 , all in smaller volumes compared to local galaxies (e.g., Erb et al. 2006b; Law et al. 2012; Tacconi et al. 2013). However, understanding the physical cause of the differences in their nebular spectra has proven both challenging and controversial (cf. Masters et al. 2014, 2016; Steidel et al. 2014; Sanders et al. 2016), with much of the difficulty stemming from the diversity (and degeneracy) of possible explanations. The differences between nebular diagnostics observed at $z \sim 2$ relative to $z \sim 0$ can be attributed to differences in the underlying stellar populations (e.g., EUV ionizing spectrum, main sequence lifetime, metallicity, binarity, rotation) and/or differences in the conditions of the interstellar medium (ISM; e.g., density, temperature, metallicity).

From our analysis of the initial Keck Baryonic Structure Survey (KBSS)-MOSFIRE sample of ~ 200 $z \simeq 2.3$ galaxies in Steidel et al. (2014, hereafter S14), we concluded that the high-redshift locus of galaxies in the N2-BPT plane is most easily explained by a harder stellar ionizing radiation field than applies to galaxies occupying the low-redshift sequence, accompanied by slightly elevated ranges in ionization parameter U ($\equiv n_\gamma/n_H$) and electron density (n_e). In S14 we noted that the systematic offset of high- z galaxies relative to star-forming galaxies in the low-redshift universe in the N2-BPT plane cautions against using the common “strong-line” metallicity relations (generally calibrated using galaxy and H II region samples at $z \sim 0$) for high-redshift galaxies, since the calibrations are designed to reproduce the local N2-BPT sequence. Additionally, an important consequence of the high excitation of the $z \sim 2.3$ KBSS-MOSFIRE sample is that the

strong-line ratios become relatively insensitive to the ionized gas-phase oxygen abundance (often what one intends to measure) and more dependent on the spectral shape of the integrated ionizing radiation field produced by massive stars.

In S14 we also investigated the effect of differences in nitrogen-to-oxygen abundance ratio on the rest-optical nebular spectra of high- z galaxies, but ultimately found that systematically different values of N/O between $z \sim 2.3$ and $z \sim 0$ galaxies were not required to reproduce the observed N2-BPT offset using the photoionization models presented in that paper. Other recent work based on independent (but smaller) galaxy samples at similar redshifts (Masters et al. 2014, 2016; Shapley et al. 2015; Cowie et al. 2016; Sanders et al. 2016) has argued that high-redshift objects have higher N/O at a given O/H—that is, the N2-BPT offset is primarily a shift toward higher $[\text{N II}]/\text{H}\alpha$ and is confined to lower-mass galaxies in those samples. The primary basis for this assertion is that an offset of the BPT locus is observed in $[\text{N II}]/\text{H}\alpha$ but not in $[\text{S II}]/\text{H}\alpha$. However, the behavior of N/O versus O/H for many individual galaxies at high redshift has yet to be established.

Although much can be learned from rest-optical nebular spectra regarding the properties of the ISM and massive stars, it is not clear that the physical factors most important for determining the location of typical local star-forming galaxies in the nebular diagnostic diagrams are the same as those at $z \sim 2$. The goal of this paper is to leverage measurements from the rest-optical spectra of an expanded sample of $\langle z \rangle = 2.3$ KBSS-MOSFIRE galaxies to characterize the properties of high- z galaxies in terms of their stellar masses, SFRs, ionization and excitation conditions, electron densities, and the variation in N/O as a function of O/H. We will show that the seemingly discrepant behavior in the N2-BPT and S2-BPT diagrams (and other diagnostic line ratios) is expected in the context of physically motivated photoionization models anchored by observations of the rest-UV spectra of the same galaxies (Steidel et al. 2016, hereafter S16).

The remainder of this paper is structured as follows: Section 2 describes the KBSS, the near-infrared spectroscopic observations, and the detailed spectral fitting of the data. Section 3 reports the measurements of strong-line ratios from the nebular spectra of KBSS-MOSFIRE galaxies. Section 4 examines the properties of $z \sim 2.3$ galaxies as a function of their offset from the $z \sim 0$ relation in the N2-BPT diagram. Section 5 presents the N/O measurements and their correlation with galaxy properties. Section 6 describes the inferences that can be made by comparing a subset of the photoionization models from S16 with the observed line ratios and inferred abundance ratios. Finally, Section 7 revisits the nature of the BPT “offset” in the context of the KBSS-MOSFIRE results. The conclusions are summarized in Section 8.

Throughout the paper, we assume a Λ CDM cosmology when necessary, with $H_0 = 70 \text{ km s}^{-1} \text{ Mpc}^{-1}$, $\Omega_\Lambda = 0.7$, and $\Omega_m = 0.3$. Stellar masses and SFRs are reported assuming a Chabrier (2003) stellar initial mass function (IMF). When a solar metallicity scale is needed for comparison, we adopt $12 + \log(\text{O}/\text{H})_\odot = 8.69$, $\log(\text{N}/\text{O})_\odot = -0.86$, and $Z_\odot = 0.0142$ (Asplund et al. 2009). Specific spectral features are referred to using their vacuum wavelengths.

2. The Keck Baryonic Structure Survey

The KBSS (Rudie et al. 2012; Steidel et al. 2014) is a large, targeted spectroscopic survey designed to jointly probe

galaxies and their gaseous environments at the peak of galaxy assembly, $z \simeq 2$ –3. The survey comprises 15 independent fields, with a total survey area of 0.24 deg^2 . The galaxies themselves are selected from deep optical and near-infrared (NIR) imaging and subsequently followed up with spectroscopic observations in the rest-UV with the Low Resolution Imaging Spectrometer (LRIS, Oke et al. 1995; Steidel et al. 2004) and, since 2012 April, in the rest-optical with the MOSFIRE (McLean et al. 2012; Steidel et al. 2014).

In addition to the physical motivation for studying galaxies at $z \simeq 2$ –3, this redshift range also offers important practical advantages: many of the strong rest-optical (3600–7000 Å) nebular emission lines originating in the galaxies’ H II regions are well-positioned with respect to the J , H , and K band atmospheric windows. Additionally, the rest-frame far-ultraviolet (1000–2000 Å) spectra of the same galaxies are accessible to ground-based telescopes, which is critically important for complementary studies of their massive stellar populations, which is one of the main goals of our recent work in S16 and is discussed briefly in Section 6.

2.1. Photometry and Sample Selection

The photometric data available in the KBSS fields have been described in detail elsewhere (e.g., by Steidel et al. 2004; Reddy et al. 2012; Steidel et al. 2014). To summarize, all of the survey regions have optical imaging in the U_n , G , and \mathcal{R} bands, as well as broadband NIR imaging in J and K_s . For 14 fields, imaging was also obtained using *Spitzer*/IRAC (typically including coverage in two channels per field); 10 fields have at least one deep pointing obtained using *Hubble*/WFC3-IR F160W; and intermediate-band NIR imaging in $J1$, $J2$, $J3$, $H1$, and $H2$ was collected using *Magellan*-FourStar (Persson et al. 2013) for 8 fields accessible from the southern hemisphere.

The majority of KBSS galaxies are selected by their rest-UV colors, based on a $U_n G \mathcal{R}$ color selection designed to identify Lyman Break Galaxy analogues at $z \simeq 2$ –2.7 (Adelberger et al. 2004; Steidel et al. 2004). However, this rest-UV color selection may be biased against massive galaxies and galaxies whose UV continua are heavily reddened due to extinction by dust ($E(B - V)_{\text{cont}} > 0.3$). Fortunately, these biases can be mitigated by using information about the combined rest-UV and rest-optical shape of the galaxies’ spectra. The 4000 Å and Balmer breaks, which probe both age and stellar mass, lie within the J band at $z \sim 2.3$ but are still well-traced by $\mathcal{R} - K_s$ color. Therefore, combining a $U_n G \mathcal{R}$ color selection with a $(\mathcal{R} - K_s)_{\text{AB}} > 2$ color cut preferentially selects galaxies at the redshifts of interest that occupy the high end of the stellar mass distribution. We also extend the optical color selection to include sources with redder $U_n G \mathcal{R}$ colors and simultaneously impose a $\mathcal{R} - K_s$ cut in order to identify galaxies that may be at similar redshifts but are scattered out of the Steidel et al. (2004) selection windows due to the effects of substantial reddening by dust.

We defer a more detailed description of this sample of galaxies—referred to as “RK” objects—and their effect on the stellar mass-completeness of the KBSS-MOSFIRE sample to a forthcoming paper (A. Strom et al. 2017, in preparation), but Figure 1 offers a visual illustration of the color selection windows described here. With the inclusion of RK objects, the KBSS targets sources throughout the full rest-UV color space occupied by high- z galaxies. Although the sample only

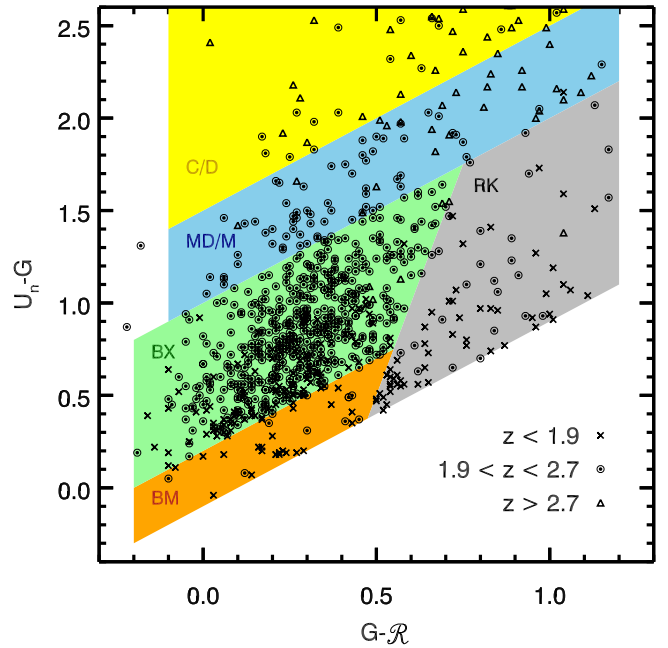


Figure 1. The optical color selection windows from Steidel et al. (2004) used to identify candidate star-forming galaxies with $z \simeq 2.0$ –2.7 (“BX” in green) and $z \simeq 2.7$ –3.4 (“MD/M” and “C/D” in blue and yellow, respectively); the gray region indicates the new “RK” color selection at redder $G - \mathcal{R}$ colors. Black symbols represent spectroscopically confirmed galaxies in KBSS-MOSFIRE sample, with the symbol shape indicating the nebular redshift.

includes galaxies with $\mathcal{R} < 25.5$ (\mathcal{R} samples the rest-frame at ~ 2100 Å), the color selection allows for galaxies with significantly fainter rest-frame FUV emission to be selected, down to an AB magnitude of 26.7 in G band ($\lambda_e \sim 1500$ Å at $z \sim 2.3$).

2.2. NIR Spectroscopic Observations

S14 introduced the NIR spectroscopic observations of KBSS galaxies with MOSFIRE, and readers are referred to Section 2 of that paper for details related to data acquisition and reduction. One particularly salient aspect of the KBSS-MOSFIRE observing strategy is that due to the dense spatial sampling of the KBSS fields, multiple slitmask configurations in each band are usually required to obtain observations of all high-priority targets in a given field. Because galaxies remain on masks until the strongest lines ($H\alpha$, $[\text{N II}]\lambda 6585$, $[\text{O III}]\lambda 5008$ $H\beta$, and $[\text{O II}]\lambda\lambda 3727, 3729$) are measured with $S/N > 5$, an individual galaxy is often observed at least twice in a single band. Section 2.4 describes the method used to correct observations of KBSS-MOSFIRE galaxies for slit losses, which takes advantage of the multiple observations of individual galaxies that result from this survey strategy.

As of 2016 May, 1060 KBSS galaxies have been confirmed spectroscopically with observations from MOSFIRE (Figure 2); of these, 733 are in the primary targeted redshift range $1.9 \lesssim z \lesssim 2.7$, with the remainder split roughly 2:1 between $1.3 \lesssim z \lesssim 1.7$ and $z \gtrsim 2.9$. The majority of the $z \sim 2.3$ galaxies have been observed in at least two NIR bands, and 279 have high-quality observations in J , H , and K band, providing good S/N measurements of most of the strong rest-optical emission lines: $[\text{O II}]\lambda\lambda 3727, 3729$, $[\text{Ne III}]\lambda 3869$ in J band; $H\beta$, $[\text{O III}]\lambda\lambda 4960, 5008$ in H band; $[\text{N II}]\lambda\lambda 6549, 6585$, $H\alpha$, $[\text{S II}]\lambda\lambda 6718, 6732$ in K band.

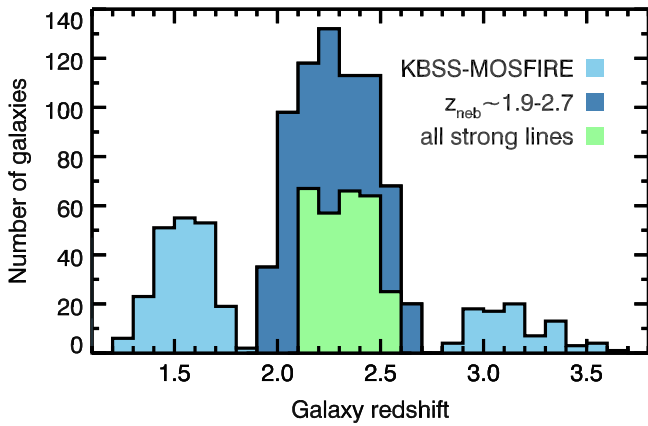


Figure 2. The redshift distribution of spectroscopically confirmed KBSS-MOSFIRE galaxies, as of 2016 May. The blue histograms represent galaxies with confirmed nebular redshifts from MOSFIRE observations (1060 total). Of these, 733 are known to be at $1.9 \leq z \leq 2.7$ and have MOSFIRE observations covering at least one atmospheric band (dark blue). The subsample with good signal-to-noise detections of strong rest-optical emission lines in J , H , and K band is shown in green (279 galaxies).

2.3. Interactive 1D Spectral Extraction and Emission Line Fitting with MOSPEC

The two-dimensional (2D) spectrograms produced by the MOSFIRE data reduction pipeline⁶ are flux-calibrated and corrected for telluric absorption using wide- and narrow-slit observations of A0V stars and then shifted to account for the heliocentric velocity at the start of each exposure sequence. Separate MOSFIRE observations of the same object are combined using inverse-variance weighting to produce the final 2D spectrograms from which 1D spectra are extracted.

One-dimensional (1D) spectra are extracted from the 2D spectrograms using MOSPEC, an interactive analysis tool developed in IDL specifically for MOSFIRE spectroscopy of faint emission line galaxies. By default, MOSPEC uses a boxcar extraction aperture (determined by the user, with a median value of 10 pixels or $1''.80$, corresponding to 14.8 kpc at $z = 2.3$). Other extraction algorithms, including optimal extraction, were tested and found not to significantly impact the measured line fluxes or their significance.

As part of the extraction process, the 1D spectrum is simultaneously fit for the redshift, line width, and fluxes of a user-specified list of emission lines. The continuum level is estimated using a reddened high-resolution stellar population synthesis model (from Bruzual & Charlot 2003) that best matches the full spectral energy distribution (SED) of the galaxy and is scaled to match the median level of the observed spectrum, excluding regions $< 5 \text{ \AA}$ from strong emission lines. This method self-consistently accounts for the effects of age and dust extinction on the underlying stellar continuum. If this method is not possible (most frequently due to very faint continua), MOSPEC uses a linear fit to the continuum, again excluding regions around strong emission lines. These two estimates agree well for most galaxies, although the model-continuum method has the advantage of including the stellar Balmer absorption features.

The correction for absorption in $H\alpha$ and $H\beta$ for individual objects is determined by fitting the galaxy spectrum with a modified SED model continuum that linearly interpolates

between the continuum on either side of regions around Balmer features and comparing the result with measurements from the full fit that includes stellar absorption features. For the $\sim 13\%$ of the sample where a stellar continuum model could not be used to automatically correct the measured line fluxes, we assume a multiplicative correction of $C_{H\beta} = 1.06$, the median of the measured corrections. No correction is applied to $H\alpha$ (although formally the median measured correction is $C_{H\alpha} = 1.01$).

The emission lines are fit using Gaussian profiles with a single redshift (z) and observed velocity width (σ , in km s^{-1}) in a given band (i.e., all lines in the K band spectrum are fit with a single z and σ , but these may differ from the parameters measured in J or H band). For objects with observations covering H and K band, $\langle |\Delta z_{H-K}| \rangle = 2 \times 10^{-4}$ ($\Delta v \approx 18 \text{ km s}^{-1}$) and $\langle \frac{|\Delta \sigma_{H-K}|}{\sigma_H} \rangle = 0.22$. For 19% of galaxies with observations covering J band, the redshift was fixed to match the redshift observed in H or K band to ensure an accurate measurement of the $[\text{O II}]$ doublet ratio in cases where the lines are only partially resolved; for all other objects, $\langle |\Delta z_{K-J}| \rangle = 4 \times 10^{-4}$ and $\langle |\Delta z_{H-J}| \rangle = 4 \times 10^{-4}$. Except for emission lines with particularly high signal-to-noise ($S/N \sim 50$), the Gaussian approximation agrees with the directly integrated flux (summed over a range $\pm 3\sigma$ as defined by the fitted velocity width) at the few percent level. The ratios of the nebular $[\text{O III}]\lambda\lambda 4959, 5008$ and $[\text{N II}]\lambda\lambda 6549, 6585$ doublets are fixed at 1:3, and the ratios of the density-sensitive $[\text{O II}]\lambda\lambda 3727, 3729$ and $[\text{S II}]\lambda\lambda 6718, 6732$ doublets are restricted to be within 20% of the range of physically allowed values, which is 0.43–1.5 for $[\text{S II}]\lambda 6718/[\text{S II}]\lambda 6732$ (Tayal & Zatsarinny 2010; Mendoza & Bautista 2014) and 0.35–1.5 for $[\text{O II}]\lambda 3729/[\text{O II}]\lambda 3727$ (Kisielius et al. 2009). The 1σ errors on all measurements account for uncertainties in the fit parameters, as well as covariance between parameters.

2.4. Slit-loss Corrections

Because some rest-frame optical diagnostics rely on ratios of emission lines widely separated in wavelength, it is important to ensure that the relative flux-calibration between the NIR atmospheric bands is correct for individual objects. For example, without such cross-calibration, extinction corrections using the Balmer decrement are impossible, as $H\beta$ falls in H band and $H\alpha$ falls in K band for galaxies at $z \simeq 2\text{--}2.7$.

The overall atmospheric transparency and image quality for each MOSFIRE mask are monitored using concurrent observations of a bright star placed in a dedicated slit (with all slit widths = $0''.7$), and an initial guess at the slit-loss correction factor for observations from that mask is determined by comparing the measured flux of the star with its broadband photometry. At the typical seeing (between $0''.5$ and $0''.7$), most science targets are unresolved or only marginally resolved. However, there are still several factors that can affect the throughput of sources differently, depending on their physical size and location on the mask, including minor glitches in tracking the rotation of high-elevation pointings and “slit drift” due to the combined effects of differential atmospheric refraction and differential flexure of the guider field relative to the science field. Consequently, it is important to optimize the mask correction factors for all objects on a given mask in a given atmospheric band, rather than rely exclusively on the correction determined using observations of the bright comparison star.

⁶ <http://www2.keck.hawaii.edu/inst/mosfire/drpf.html>

Optimal mask correction factors are calculated for all individual masks (213 total) using a Markov Chain Monte Carlo (MCMC) routine. The MCMC routine searches parameter space for the combination of individual mask correction factors that minimizes the scatter between independent measurements of strong lines (typically $H\alpha$, $[O\text{ III}]\lambda 5008$, or the sum of the $[O\text{ II}]\lambda\lambda 3727, 3729$ doublet) in galaxies' spectra, as many galaxies are observed more than once in a given band. The routine uses the comparison star measurements to construct priors on the mask corrections, which are allowed to sample a range from 1 to 3.5, chosen empirically to coincide with the range of corrections observed for the comparison stars. In cases where an individual mask includes observations of more than one bright star, the preliminary correction factors are compared to ensure good agreement. Outlier rejection is performed on a mask-by-mask basis prior to initializing the chain by censoring individual galaxies that require an anomalously high or low correction factor relative to other galaxies on the same mask. The principal advantage of using this method to solve for the mask correction factors in parallel is that it provides a quantitative measure of how well or how poorly a single mask correction factor performs for all objects observed on a mask and provides the means to flag masks with unreliable correction factors based on the shape of the posterior distribution.

On average, the posteriors for the mask corrections are positively skewed, and $\sim 60\%$ of masks exhibit a significant degree of skewness (positive or negative). As a result, the characteristic value for a given mask correction is taken to be the center of the 68% highest posterior density interval rather than the mean value, with the width of the interval representing the uncertainty in the mask correction determination.

For galaxies observed on a single mask, the optimal mask correction is used to correct the measured line fluxes. When a galaxy has been observed more than once, line fluxes from the 2D weighted average spectrum are corrected to match the weighted average of the corrected line flux measurements from the constituent 2D spectral observations; the scatter around the average is the reported uncertainty on the individual object slit correction. The statistics of the 826 individual measurements of galaxies and their uncertainties are presented in Figure 3; the median slit-loss correction factor is 2.03, with a median uncertainty of 8%.

2.5. Stellar Masses and SFRs

Stellar mass (M_*) estimates for galaxies in the KBSS-MOSFIRE sample are inferred from reddened stellar population synthesis models fit to broadband photometry, as described by Reddy et al. (2012) and S14. The SED fitting employs solar metallicity models from Bruzual & Charlot (2003), a Chabrier (2003) IMF, the Calzetti et al. (2000) attenuation curve, and constant star formation histories for all galaxies, with a minimum allowed age of 50 Myr. This age is a dynamically reasonable minimum imposed to prevent best-fit solutions with unrealistically young ages, as discussed by Reddy et al. (2012). Typical uncertainties in $\log(M_*/M_\odot)$ are estimated to be ± 0.1 – 0.2 dex, with a median uncertainty of 0.16 dex (Shapley et al. 2005; Erb et al. 2006b).

Because SFR estimates from SED fitting are naturally correlated with other fit parameters such as age and M_* , the SFRs used for analysis of the KBSS-MOSFIRE sample in this paper are obtained from dust-corrected measurements of the

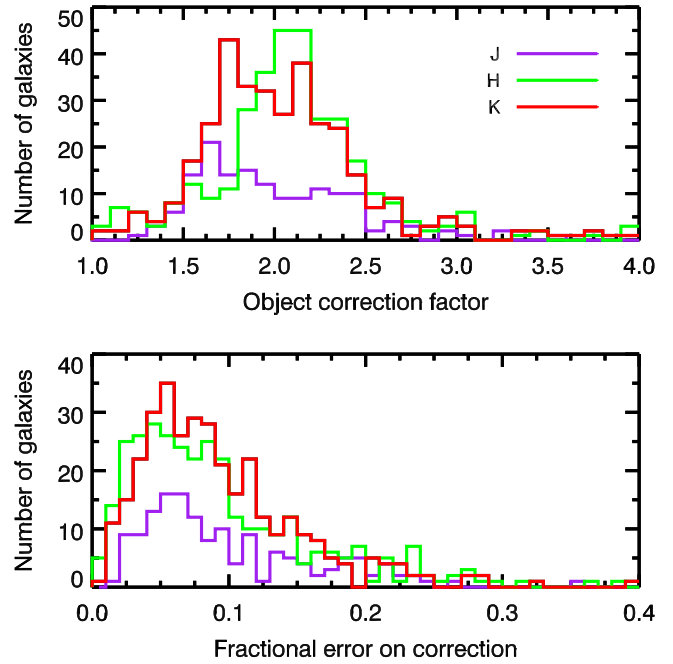


Figure 3. The distributions of individual object slit correction (top panel) and fractional error on the correction (bottom panel) broken down by NIR atmospheric band for 826 measurements of $z \sim 2.3$ KBSS-MOSFIRE galaxies. Overall, the median slit correction is 2.03, with a median uncertainty of 8%.

$H\alpha$ recombination line using the relation from Kennicutt (1998) and assuming a Chabrier (2003) IMF. Shivaie et al. (2016) reported that for $z \sim 2$ galaxies from the MOSFIRE Deep Evolution Field survey (MOSDEF, Kriek et al. 2015), $H\alpha$ -based estimates of SFR are consistent with those estimated from the full panchromatic SED (including UV and far-IR photometry). Dust extinction toward star-forming regions is estimated by comparing the Balmer decrement ($H\alpha/H\beta$) with the expected Case B value of 2.86 (Osterbrock 1989). Galaxies with Balmer decrements < 2.86 are assumed to have zero extinction, with $\sim 46\%$ of such galaxies exhibiting Balmer decrements consistent with the nominal Case B value within 3σ . Adopting the Galactic extinction curve from Cardelli et al. (1989) for galaxies with $H\alpha/H\beta \geq 2.86$, the interquartile range for extinction along the line of sight to H II regions in the full sample of $z \sim 2.3$ KBSS-MOSFIRE galaxies is $E(B - V)_{\text{neb}} = 0.06 - 0.47$, with a median value of 0.25 and a corresponding median $A_{H\alpha} = 0.63$ mag.

The distributions of M_* , $H\alpha$ -based SFR, and specific star formation rate ($s\text{SFR} \equiv \text{SFR}/M_*$) for 207 $z \sim 2.3$ KBSS-MOSFIRE galaxies with $S/N > 5$ Balmer decrement measurements are presented in Figure 4. Table 1 provides an overview of the sample statistics for the subsamples of KBSS-MOSFIRE galaxies discussed in the following sections and notes the corresponding emission line selection criteria. In cases where extinction corrections are necessary, we require the measurement of $H\alpha/H\beta$ to have $S/N > 5$, including the uncertainty from the relative slit corrections. This S/N cut is well-motivated by the fact that extinction corrections for individual emission lines scale nonlinearly with the measured value of the Balmer decrement, going approximately as $(H\alpha/H\beta)^{k_\lambda}$, where k_λ is the value of the reddening curve at a specific wavelength ($k_{H\alpha} = 2.52$ for the Cardelli et al. 1989 extinction curve). Thus even relatively small uncertainties in the Balmer decrement translate to much larger uncertainties in the corrected line ratio.

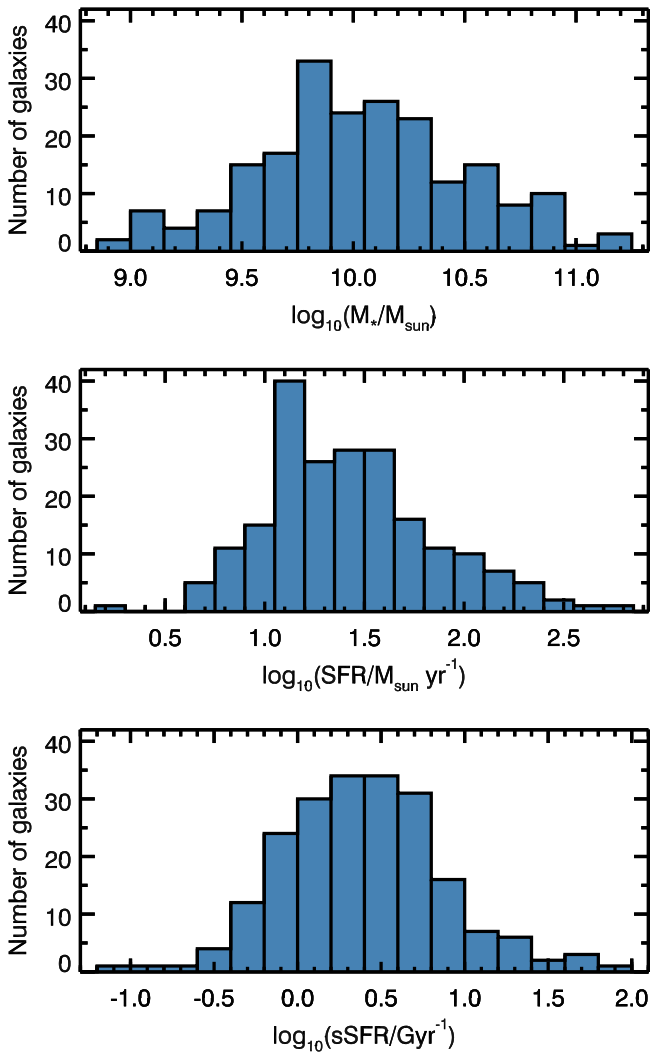


Figure 4. Stellar mass, star formation rate, and specific star formation rate distributions for 207 $z \sim 2.3$ KBSS-MOSFIRE galaxies with $S/N > 5$ Balmer decrement measurements. Stellar masses are determined from SED fits, and SFRs are calculated from dust-corrected $H\alpha$ emission line measurements. The median stellar mass is $1.0 \times 10^{10} M_{\odot}$, and the median SFR is $24 M_{\odot} \text{ yr}^{-1}$, with a median sSFR of 2.4 Gyr^{-1} .

3. Nebular Emission Line Ratios

3.1. The N2- and S2-BPT Diagrams

Figure 5 shows the location of 377 KBSS-MOSFIRE galaxies with $1.9 < z < 2.7$ ($\langle z \rangle = 2.3$) in the N2-BPT plane, including only those galaxies where $H\alpha$ is detected at $>5\sigma$ and $H\beta$ and $[\text{O III}]\lambda 5008$ are detected at $>3\sigma$ (light green points). Galaxies with $[\text{N II}]\lambda 6585$ measurements with $S/N < 2$ are assigned 2σ upper limits (dark green triangles), accounting for $\sim 36\%$ of the sample. As we originally reported in S14 for a smaller sample, KBSS-MOSFIRE galaxies occupy a region of the N2-BPT plane almost entirely distinct from the majority of local galaxies, represented by SDSS-DR8 (in grayscale, Aihara et al. 2011).

The SDSS comparison sample employed in this paper takes emission line measurements and ancillary physical parameters from the MPA-JHU catalogs⁷ (cf. Sections 4.3.1 and 4.3.2 of Aihara et al. 2011) and has been selected to be similar to

KBSS-MOSFIRE in terms of detection properties. The SDSS comparison galaxies have $0.04 \leq z \leq 0.1$ (to avoid severe aperture effects), $>50\sigma$ measurements of $H\alpha$, and a “reliable” flag signaling good results from the MPA-JHU pipeline. Stellar masses, SFRs, and sSFRs are reported using the median estimates of the PDFs for the “total” values.

Although the existence of an offset in the N2-BPT plane has been widely reported for other samples of high-redshift galaxies (Masters et al. 2014; Shapley et al. 2015; Sanders et al. 2016), the degree to which the KBSS-MOSFIRE sample differs from typical local galaxies is quite remarkable. Nearly all KBSS-MOSFIRE galaxies have larger values of $\log([\text{O III}]/H\beta)$ at fixed $\log([\text{N II}]/H\alpha)$ than typical SDSS galaxies in the N2-BPT diagram (represented by the 90% of $z \sim 0$ galaxies enclosed by the orange contour in Figure 5). Furthermore, the ridge-line of the $z \sim 2.3$ sample with $>2\sigma$ detections of $[\text{N II}]\lambda 6585$, traced by median values of $\log([\text{O III}]/H\beta)$ in equal-number bins of $\log([\text{N II}]/H\alpha)$ (yellow stars; Table 2), falls well outside the same contour.

The N2-BPT locus can be described analytically using the following functional form:

$$\log([\text{O III}]/H\beta) = \frac{p_0}{\log([\text{N II}]/H\alpha) + p_1} + p_2. \quad (1)$$

However, because the fit parameters are degenerate, interpreting them is difficult. To be consistent with the literature, we fit the KBSS-MOSFIRE locus with p_0 fixed to the value reported by Kewley et al. (2001) for the N2-BPT extreme starburst classification line ($p_0 = 0.61$). We determine the best-fit curve describing the KBSS-MOSFIRE N2-BPT locus (cyan curve in Figure 5) using the IDL routine MPFIT (Markwardt 2009), with the following result:

$$\log([\text{O III}]/H\beta) = \frac{0.61}{\log([\text{N II}]/H\alpha) - 0.22} + 1.12. \quad (2)$$

The intrinsic scatter relative to the best-fit curve is 0.18 dex, estimated from the amount of additional uncertainty required to achieve $\chi^2/\text{DOF} = 1$ after accounting for individual measurement errors. Galaxies with upper limits on $[\text{N II}]$ and objects identified as AGN (magenta squares; see also Section 3.2) are excluded from the fit.

We determine the $z \sim 0$ locus for the SDSS comparison sample using the same form (red dashed line), including only star-forming galaxies identified using the Kauffmann et al. (2003) selection. When p_1 and p_2 are fixed separately, we find that the observed offset between the $z \sim 0$ N2-BPT locus and the KBSS-MOSFIRE ridge-line can be described by a shift of either

$$\begin{aligned} \Delta \log([\text{O III}]/H\beta) &= 0.26 \text{ dex or} \\ \Delta \log([\text{N II}]/H\alpha) &= 0.37 \text{ dex.} \end{aligned}$$

Even when p_0 is treated as a free parameter, the amplitudes of these shifts are similar, so long as the same p_0 is adopted for both the low- z SDSS and high- z KBSS-MOSFIRE samples.

The difference between $z \sim 0$ and $z \sim 2.3$ galaxies observed in the S2-BPT diagram (Figure 6) is less notable than in the N2-BPT plane, a result that was previously shown by Masters et al. (2014) for stacked spectra and by Shapley et al. (2015) and Sanders et al. (2016) for individual high- z galaxies from the MOSDEF survey. The KBSS-MOSFIRE galaxies appear to trace the high $[\text{O III}]/H\beta$ tail of SDSS, although with larger

⁷ https://www.sdss3.org/dr10/spectro/galaxy_mpa_jhu.php

Table 1
KBSS-MOSFIRE Samples Used for Line-ratio Analysis

Subsample	N	$\langle z \rangle$	M_*^a (M_\odot)	SFR ^a ($M_\odot \text{ yr}^{-1}$)	Emission Line Criteria	Notes
N2-BPT	377	2.31	1.09×10^{10}	23.6	$H\alpha \geq 5\sigma$, $H\beta$, $[\text{O III}]\lambda 5008 \geq 3\sigma$, $[\text{N II}]\lambda 6585$ observed	b,c
S2-BPT	370	2.30	1.13×10^{10}	23.5	$H\alpha \geq 5\sigma$, $H\beta$, $[\text{O III}]\lambda 5008 \geq 3\sigma$, $[\text{S II}]\lambda\lambda 6718, 6733$ observed	c
O32-R23	171	2.35	9.49×10^9	22.9	$H\alpha \geq 5\sigma$, $H\beta$, $[\text{O III}]\lambda 5008$, $[\text{O II}]\lambda\lambda 3727, 3729 \geq 3\sigma$	c,d
N/O	151	2.34	9.94×10^9	23.5	$H\alpha \geq 5\sigma$, $H\beta$, $[\text{O II}]\lambda\lambda 3727, 3729 \geq 3\sigma$, $[\text{N II}]\lambda 6585$ observed	c,d
Ne3O2	69	2.33	7.14×10^9	22.6	$H\alpha \geq 5\sigma$, $H\beta$, $[\text{O III}]\lambda 5008$, $[\text{O II}]\lambda\lambda 3727, 3729$, $[\text{Ne III}]\lambda 3869 \geq 3\sigma$,	c,d

Notes.

^a Median values.

^b S14 used $H\alpha \geq 5\sigma$, $H\beta \geq 3\sigma$, $[\text{O III}]\lambda 5008 \geq 5\sigma$, $[\text{N II}]\lambda 6585$ observed, taken as an upper limit when the S/N < 2.

^c We adopt 2σ upper limits for emission lines without a listed S/N threshold and $< 2\sigma$ significance.

^d Emission line errors incorporate uncertainties in the slit-loss corrections, and the Balmer decrement must have S/N > 5.

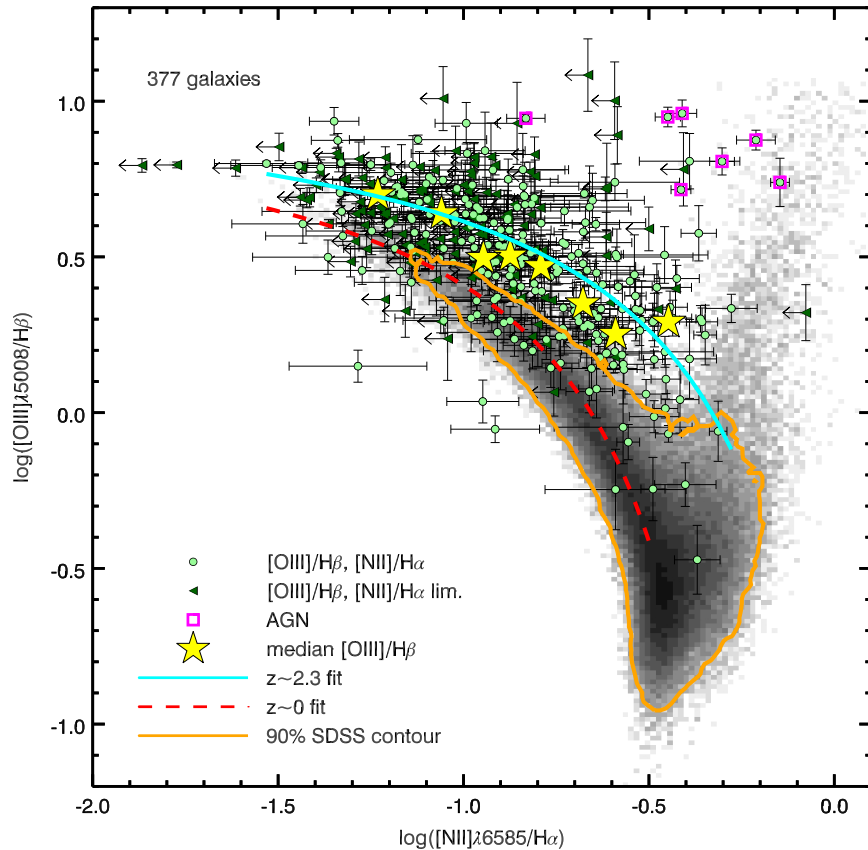


Figure 5. KBSS-MOSFIRE galaxies in the N2-BPT plane, compared with local galaxies from SDSS (in grayscale, with the orange contour enclosing 90% of the total sample). KBSS-MOSFIRE galaxies with $> 2\sigma$ detections of $[\text{N II}]\lambda 6585$ are plotted in light green, with 2σ upper limits shown instead as dark green triangles. Magenta squares denote objects identified as AGN/QSOs. The ridge-line of the high- z locus occurs far outside the 90% SDSS contour, demonstrated not only by the location of the median $\log([\text{O III}]\lambda 5008/\text{H}\beta)$ values in equal-number bins of $\log([\text{N II}]\lambda 6585/\text{H}\alpha)$ (yellow stars; see also Table 2), but also by the formal fit to the distribution of KBSS-MOSFIRE galaxies (cyan curve). The $z \sim 0$ locus is represented by the red dashed curve.

scatter due to measurement errors. The best fit to the S2-BPT locus (cyan curve in Figure 6) with $p_0 = 0.72$ (Kewley et al. 2001) grazes the upper edge of the distribution of local galaxies, taking the form

$$\log([\text{O III}]/\text{H}\beta) = \frac{0.72}{\log([\text{S II}]/\text{H}\alpha) - 0.53} + 1.15, \quad (3)$$

with an intrinsic scatter of 0.22 dex. Note that the median values of $\log([\text{O III}]/\text{H}\beta)$ in equal-number bins of $\log([\text{S II}]/$

$\text{H}\alpha)$ (yellow stars) also lie close to the upper envelope of the orange contour enclosing 90% of SDSS galaxies.

As we will discuss in Section 5.3, the same behavior persists when one compares the $z \sim 2.3$ KBSS-MOSFIRE sample with SDSS galaxies that have similar ionization and excitation properties: the KBSS-MOSFIRE sample exhibits a substantial offset relative to SDSS in the N2-BPT plane, but virtually no separation is observed in the S2-BPT diagram. In Section 6, we show that the same self-consistent photoionization models can explain the observations in both cases.

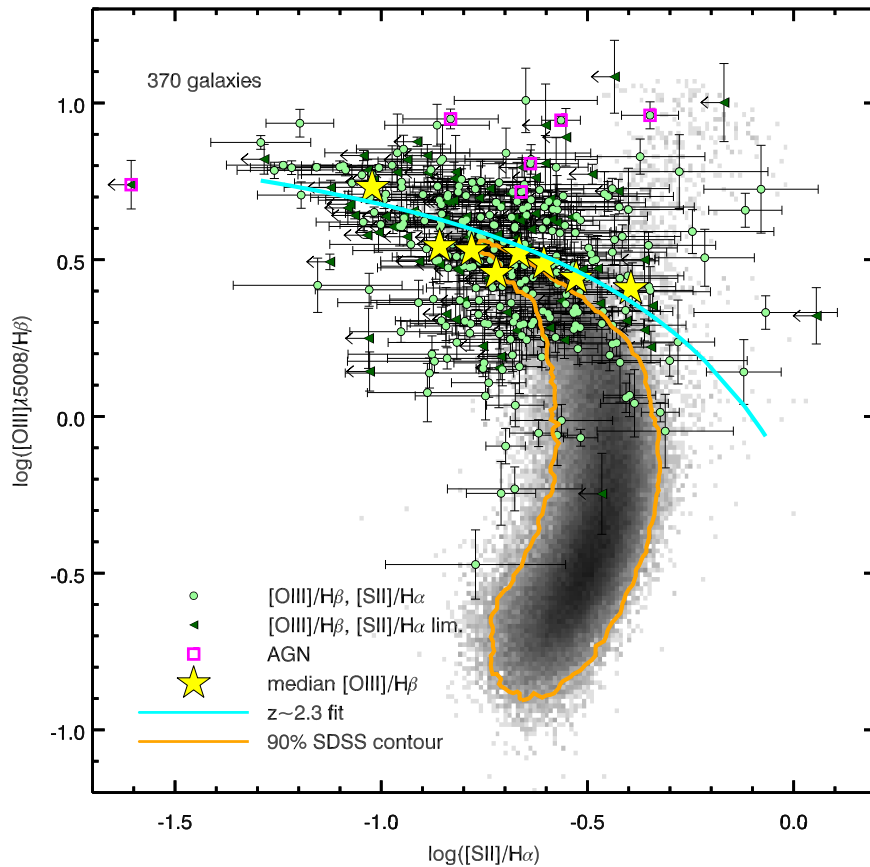


Figure 6. The S2-BPT diagram displayed in the same manner as Figure 5. Note that while $z \sim 2.3$ galaxies are noticeably offset relative to the $z \sim 0$ sample in the N2-BPT diagram, a similar offset is not observed in the S2-BPT plane. Instead, the $\log([\text{O III}]/\text{H}\beta)$ medians (yellow stars; Table 2) and the fit to the KBSS-MOSFIRE locus (cyan curve) coincide with the upper envelope of the orange contour, which encloses 90% of SDSS galaxies.

Table 2
Median Line Ratios

N2-BPT		S2-BPT	
$\log[\text{N II}]/\text{H}\alpha$	$\log[\text{O III}]/\text{H}\beta$	$\log[\text{S II}]/\text{H}\alpha$	$\log[\text{O III}]/\text{H}\beta$
-1.23	0.70	-1.02	0.73
-1.06	0.64	-0.86	0.54
-0.95	0.50	-0.78	0.53
-0.87	0.50	-0.72	0.46
-0.79	0.47	-0.67	0.52
-0.68	0.35	-0.61	0.49
-0.59	0.25	-0.53	0.44
-0.45	0.29	-0.39	0.41

Note. These values of $\log[\text{O III}]/\text{H}\beta$ are the medians in equal-number bins of $\log[\text{N II}]/\text{H}\alpha$ and $\log[\text{S II}]/\text{H}\alpha$, where only galaxies with $>2\sigma$ detections of $[\text{N II}]\lambda 6585$ or $[\text{S II}]\lambda\lambda 6718, 6732$ have been included. The reported values of $\log[\text{N II}]/\text{H}\alpha$ and $\log[\text{S II}]/\text{H}\alpha$ are the median values of those quantities in each bin.

3.2. AGN Contamination

Given the differences observed in the N2-BPT diagram between $z \sim 2.3$ galaxies and local star-forming galaxies, it is important to understand the risk of AGN contamination, which could lead to misinterpretation of the results described previously. Although the BPT diagrams are used to separate star-forming galaxies and AGN at low- z , a similar application at high redshift is less straightforward. Kewley et al. (2013) used photoionization models to explore differences in the BPT

plane at higher redshifts and noted that the distinct “branches” seen in the N2-BPT diagram become less discernible with changes in ISM conditions and AGN properties. From observations alone, the problem is also clear: the majority of $z \sim 2.3$ KBSS galaxies fall in the region of the N2-BPT diagram (Figure 5) generally reserved for “composite” objects—those that show signs of AGN activity as well as ongoing star formation—at $z \sim 0$.

We considered this issue in some detail in S14, but summarize it again here. KBSS galaxies are flagged as AGN or QSOs if (1) their rest-UV (LRIS) spectrum shows significant emission in high ionization lines (such as $\text{C IV}\lambda 1549$, $\text{C III}\lambda 1908$, $\text{N V}\lambda 1240$; Hainline et al. 2011) or (2) a combination of their rest-optical emission line ratios and line widths suggest the presence of an AGN. These objects (seven in total) generally fall near the upper envelope of $\log([\text{O III}]/\text{H}\beta)$ observed for KBSS galaxies and in the upper half of the stellar mass range sampled by the survey; they are excluded from fits to the galaxy sample (including those reported in Section 3.1) and from analyses that require extinction corrections.

3.3. The Stellar Mass-excitation Relation

Similar to the offset observed in the N2-BPT plane, the behavior of $[\text{O III}]/\text{H}\beta$ with respect to M_* (referred to as the MEx; Juneau et al. 2011) highlights dramatic differences between $z \sim 2.3$ KBSS-MOSFIRE galaxies and local galaxies

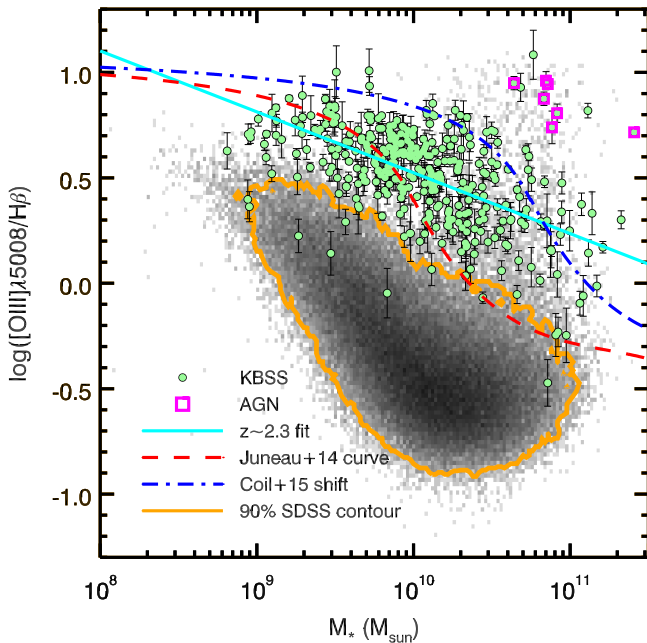


Figure 7. The mass-excitation relation (MEx) for 365 KBSS-MOSFIRE galaxies with M_* estimates (green) and SDSS galaxies (grayscale), with the division between star-forming/composite galaxies and AGN in the local universe from Juneau et al. (2014) illustrated by the red dashed curve. The dotted-dashed blue curve represents the shift proposed by Coil et al. (2015) to separate $z \sim 2$ star-forming galaxies from AGN. KBSS-MOSFIRE galaxies identified as AGN are denoted by magenta squares. The correlation between $[\text{O III}]\lambda 5008/\text{H}\beta$ and M_* is one of the strongest observed for the KBSS-MOSFIRE sample (with the best-fit linear relation shown by the cyan line) and also highlights one of the largest differences between $z \sim 2.3$ galaxies and those at $z \sim 0$.

from SDSS. Figure 7 shows the M_* -excitation relation for both samples.

As for local galaxies (grayscale in Figure 7), $z \sim 2.3$ KBSS-MOSFIRE galaxies (green points) exhibit a significant inverse correlation between $[\text{O III}]\lambda 5008/\text{H}\beta$ and M_* , with a Spearman correlation coefficient of $\rho = -0.47$ and $p = 1.4 \times 10^{-21}$. However, the distribution of the $z \sim 2.3$ sample is almost entirely disjoint with respect to the majority of SDSS galaxies (enclosed by the 90% contour in orange), with 82% of KBSS-MOSFIRE objects falling above the updated curve from Juneau et al. (2014) used to divide star-forming/composite galaxies from AGN in the local universe (red dashed curve in Figure 7). This empirical division was calibrated using $z \sim 0.1$ SDSS galaxies and designed to function as an alternative method of distinguishing between AGN and star-forming (or composite) galaxies when not all of the BPT lines are available. Figure 7 also shows that AGN in the KBSS-MOSFIRE sample are offset to even higher $[\text{O III}]\lambda 5008/\text{H}\beta$ than the majority of the $z \sim 2.3$ galaxies at fixed M_* , although there are $z \sim 0$ AGN from SDSS that occupy the same region of parameter space. These results are largely consistent with those reported by Coil et al. (2015), who explicitly tested the success of the MEx in identifying $z \sim 2$ AGN using observations from the MOSDEF survey. In order to construct a diagnostic that more accurately distinguishes between high- z star-forming galaxies and AGN, Coil et al. (2015) proposed shifting the MEx division by $\Delta \log(M_*/M_\odot) = 0.75$, as illustrated by the dotted-dashed blue curve in Figure 7. To cleanly separate AGN from star-forming galaxies in the current KBSS-MOSFIRE sample, an even larger shift ($\gtrsim 1.0$ dex) would be required.

Table 3
Strong-line Indices

Index	Definition
N2	$\log([\text{N II}]\lambda 6585/\text{H}\alpha)$
O3N2	$\log([\text{O III}]\lambda 5008/\text{H}\beta) - \log([\text{N II}]\lambda 6585/\text{H}\alpha)$
R23	$\log([\text{O III}]\lambda\lambda 4960, 5008 + [\text{O II}]\lambda\lambda 3727, 3729)/\text{H}\beta$
O32	$\log([\text{O III}]\lambda\lambda 4960, 5008/[\text{O II}]\lambda\lambda 3727, 3729)$
N2O2	$\log([\text{N II}]\lambda 6585/[\text{O II}]\lambda\lambda 3727, 3729)$
N2S2	$\log([\text{N II}]\lambda 6585/[\text{S II}]\lambda\lambda 6718, 6732)$
Ne3O2	$\log([\text{Ne III}]\lambda 3869/[\text{O II}]\lambda\lambda 3727, 3729)$

Note. The $\lambda\lambda$ notation refers to the sum of both lines.

We calculate a linear fit to the locus of $z \sim 2.3$ KBSS-MOSFIRE star-forming galaxies in Figure 7 using the MPFITEXY IDL routine⁸ (Williams et al. 2010), and it has the form

$$\log([\text{O III}]/\text{H}\beta) = 0.52 - 0.29 \times [\log(M_*/M_\odot) - 10], \quad (4)$$

with $\sigma_{\text{RMS}} = 0.19$ dex scatter about the best-fit relation and an implied intrinsic scatter of $\sigma_{\text{int}} = 0.17$ dex. The correlation between excitation, as probed by $[\text{O III}]/\text{H}\beta$, and M_* is therefore one of the tightest correlations between the nebular spectrum and a global galaxy property.

Compared to SDSS, KBSS-MOSFIRE galaxies exhibit an offset of up to 0.8 dex toward higher $\log([\text{O III}]/\text{H}\beta)$ at fixed M_* . The largest separation occurs at the high mass end of the M_* distribution, where there are few local analogs to KBSS-MOSFIRE galaxies. Although some of the offset likely results from decreased gas-phase oxygen abundances in high- z H II regions (e.g., Pettini & Pagel 2004; Maiolino et al. 2008), we show in the following sections that the higher values of $[\text{O III}]/\text{H}\beta$ observed in $z \sim 2.3$ galaxies reflect differences in the typical shape of the ionizing radiation field in galaxies at fixed M_* as a function of redshift.

3.4. Ionization and Excitation: O32 and R23

We also consider the behavior of O32 and R23; the definitions for both indices as used in this paper can be found in Table 3, together with other strong-line indices. O32 is often employed as a proxy for ionization (Penston et al. 1990) and can be used to calculate the ionization parameter ($U \equiv n_\gamma/n_{\text{H}}$, the dimensionless ratio of the number density of incident H-ionizing photons to the number density of hydrogen atoms in the gas), given an assumed ionizing spectrum. R23 is used to estimate oxygen abundance (e.g., Pagel et al. 1979; McGaugh 1991; Kewley & Dopita 2002), although because of its double-valued nature, an additional parameter (like N2 or O3N2) must be used to break the degeneracy. R23 may also be used as a probe of the overall degree of excitation in H II regions with moderate gas-phase metallicity, as it compares the emission from two collisionally excited metallic ions (O^+ and O^{++}) with the emission from a recombination line of hydrogen, thus providing a rough constraint on the amount of kinetic energy in the gas relative to the number of ionizing photons in a similar manner to the line ratios used in the BPT diagrams.

The clear advantage of indices like O32 and R23 over the BPT ratios is that they include only one element (oxygen) in

⁸ <http://purl.org/mike/mpfitexy>

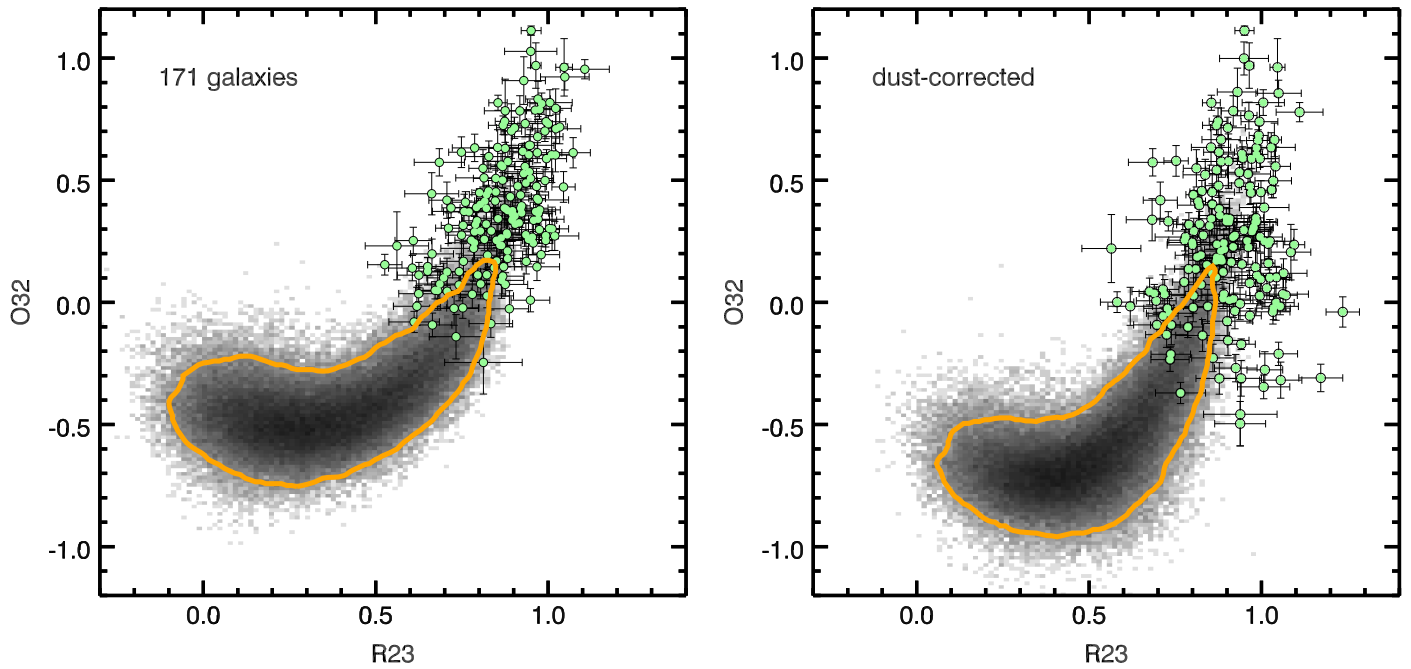


Figure 8. Left: the distribution of the O32 and R23 indices for KBSS-MOSFIRE galaxies (excluding AGN), using line fluxes that have not been corrected for dust extinction, compared with the locus of $z \sim 0$ SDSS galaxies in grayscale (the orange contour encloses 90% of the sample). Here, in contrast to earlier figures, the SDSS sample contains only star-forming galaxies, separated from AGN by the curve from Kauffmann et al. (2003). Right: the same parameter space as the left panel, but with line ratios that have been corrected for dust extinction. As in the S2-BPT diagram, KBSS-MOSFIRE galaxies largely follow the trend established by typical local galaxies, despite overlapping with only the most extreme tail of SDSS.

addition to hydrogen and should be insensitive to differences in the abundance ratio patterns of $z \sim 0$ and $z \sim 2.3$ galaxies (or, indeed, between any two populations). Moreover, unlike $[\text{O III}]/\text{H}\beta$, which is sensitive to changes in both the kinetic energy of the gas and U , R23 and O32 offer relatively independent probes of excitation and ionization, respectively. However, because both O32 and R23 require nebular extinction corrections, the indices can only be determined for $z \sim 2.3$ galaxies with observations in J , H , and K band.

Figure 8 shows $z \sim 2.3$ KBSS-MOSFIRE galaxies in the O32-R23 plane, compared with galaxies from SDSS. The left panel shows the observed ratios, corrected for relative slit losses but not for dust extinction, while the right panel shows the line ratios corrected for differential extinction due to dust as described previously in Section 2.5. The KBSS-MOSFIRE galaxies are largely coincident with the high-O32, high-R23 tail of SDSS (similar to the S2-BPT plane; Figure 6), although this region of parameter space is relatively sparsely populated by $z \sim 0$ galaxies overall, with the majority of the SDSS sample exhibiting much lower values of both indices. Similar results were also reported for $z \sim 2$ MOSDEF galaxies by Shapley et al. (2015).

This agreement reflects fundamental similarities between the most extreme SDSS galaxies and KBSS-MOSFIRE galaxies. At low gas-phase O/H, R23 increases with metallicity as the number of oxygen atoms increases; at high gas-phase O/H, R23 declines again, because the oxygen present in the gas functions as an efficient cooling pathway, reducing the gas temperature and thus the number of collisionally excited oxygen ions. Thus R23 reaches a maximum value at intermediate O/H, with the value of R23 at the turnaround depending sensitively on the hardness of the incident radiation field at fixed gas-phase O/H; a harder ionizing photon distribution will result in greater kinetic energy per ionized

electron than a softer distribution. Because there is a maximum degree of hardness for the spectra of massive stars set by stellar evolutionary processes, there is a corresponding maximum R23 achievable for star-forming galaxies, reflected in the upper envelope at $\text{R23} \sim 1$ for both samples in the right panel of Figure 8.

Thus, although there exist SDSS galaxies occupying the same high-O32, high-R23 region of parameter space as the majority of $z \sim 2.3$ galaxies, both samples must be characterized by large ionization parameters and the combination of hard ionizing radiation fields and moderate gas-phase O/H needed to produce values of R23 near the turnaround. We test this assumption in Sections 5.3 and 6.2 and evaluate the utility of the combination of O32 and R23 for determining gas-phase oxygen abundance at high redshift.

4. Physical Characteristics of the Most Offset Galaxies in the $z \sim 2.3$ N2-BPT Plane

In addition to comparing typical $z \sim 2.3$ galaxies with those commonly seen in the local universe (such as star-forming galaxies from SDSS), comparisons between high-redshift samples with different properties are also important. The latter is necessary to understand whether the physical process(es) driving the differences observed between typical galaxies at different epochs are also responsible for the diversity of galaxy properties observed at a single epoch. To facilitate this exercise, we divide the $z \sim 2.3$ KBSS-MOSFIRE galaxies into two subsamples on the basis of their position in the N2-BPT plane. High-redshift samples show the greatest deviations relative to SDSS galaxies in this parameter space, and we might therefore expect to identify correlated differences in other line ratios and physical properties between subsamples identified in such a manner.

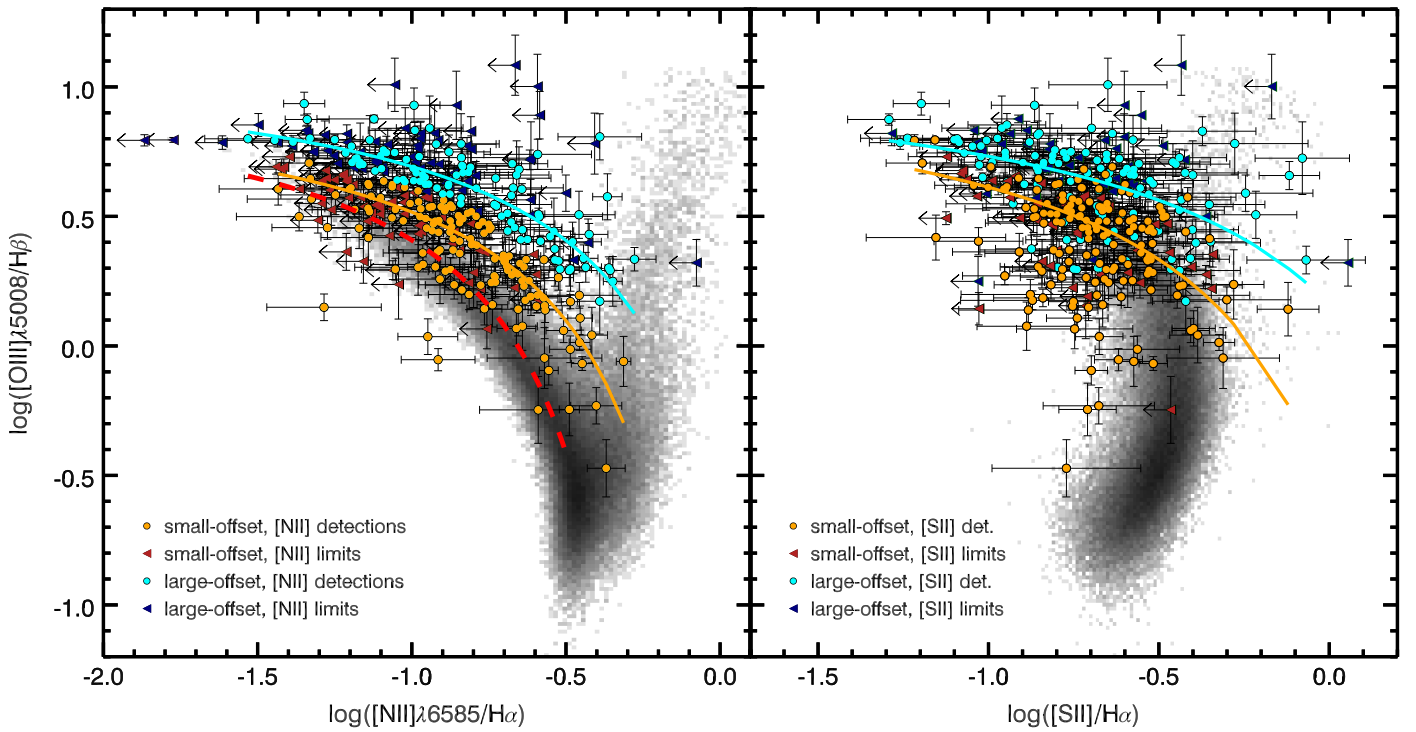


Figure 9. The N2-BPT (left) and S2-BPT (right) diagrams, showing the location of $z \sim 2.3$ KBSS-MOSFIRE galaxies color-coded on the basis of their location in the N2-BPT plane. Those falling above the KBSS ridge-line (Equation (2); cyan curve in Figure 5) are referred to as the “large-offset” subsample (cyan/navy points), and those falling below the ridge-line are instead referred to as “small-offset” galaxies (orange/red points). For reference, the $z \sim 0$ N2-BPT locus from Figure 5 is shown in red, and separate fits to the loci of both the small- and large-offset subsamples are illustrated by the solid orange and cyan curves, respectively. A comparison between the $z \sim 2.3$ loci reveals a significant shift even with respect to one another: up to $\Delta \log([\text{O III}]/\text{H}\beta) = 0.19$ dex or $\Delta \log([\text{N II}]/\text{H}\alpha) = 0.34$ dex. In the S2-BPT plane, a shift of $\Delta \log([\text{O III}]/\text{H}\beta) = 0.16$ dex or $\Delta \log([\text{S II}]/\text{H}\alpha) = 0.36$ dex would be required to bring the two loci into agreement. AGN in the KBSS-MOSFIRE sample have been excluded from both panels.

Table 4
Best-fit Parameters for BPT Ridge-lines

	p_0	p_1	p_2
SDSS N2-BPT	0.61	0.09	1.08
KBSS-MOSFIRE N2-BPT	0.61	-0.22	1.12
KBSS-MOSFIRE small-offset (N2)	0.61	-0.14	1.05
KBSS-MOSFIRE large-offset (N2)	0.61	-0.31	1.16
KBSS-MOSFIRE S2-BPT	0.72	-0.53	1.15
KBSS-MOSFIRE small-offset (S2)	0.72	-0.41	1.12
KBSS-MOSFIRE large-offset (S2)	0.72	-0.73	1.15

For the purposes of this comparison, galaxies with $\log([\text{O III}]/\text{H}\beta)$ ratios that fall above the $z \sim 2.3$ N2-BPT ridge-line (Equation (2); cyan curve in Figure 5) are designated the “large-offset” subsample, and those below the ridge-line form the “small-offset” subsample; AGN are excluded from both. Figure 9 shows the location of these two subsamples in the N2-BPT plane (where they are selected) and the S2-BPT plane. Galaxies with low-significance ($<2\sigma$) detections of $[\text{N II}]$ or $[\text{S II}]$ are identified by darker-colored triangles at the position of their 2σ upper limits. Note that if a more stringent selection is applied, such that galaxies must lie $>3\sigma$ away from the ridge-line in $\log([\text{O III}]/\text{H}\beta)$ in order to be classified as large-offset or small-offset, the nature of the results discussed as follows remains unchanged.

4.1. BPT Offsets

The loci of small-offset galaxies (orange curve in Figure 9) and large-offset galaxies (cyan curve) in the N2-BPT and S2-

BPT planes are independently fit using the method and functional form described in Section 3.1. As before, objects with upper limits on $[\text{N II}]$ or $[\text{S II}]$ are not included in determining the fits. The results for both BPT diagrams are summarized in Table 4.

Even the locus of small-offset KBSS-MOSFIRE galaxies remains noticeably different from typical SDSS galaxies in the N2-BPT plane, as shown by the offset of orange curve relative to the $z \sim 0$ locus (red dashed curve) in the left panel of Figure 9. The additional separation between the small-offset and large-offset loci is consistent with an offset of either

$$\Delta \log([\text{O III}]/\text{H}\beta)_{\text{N2}} = 0.19 \text{ dex or}$$

$$\Delta \log([\text{N II}]/\text{H}\alpha)_{\text{N2}} = 0.34 \text{ dex,}$$

if the shift is restricted to one axis.

The two subsamples are also clearly differentiated in the S2-BPT diagram (right panel of Figure 9), with large-offset galaxies exhibiting systematically higher $\log([\text{O III}]/\text{H}\beta)$ at fixed $\log([\text{S II}]/\text{H}\alpha)$ compared with the small-offset subsample. If only one fit parameter is allowed to vary, the separation between the two loci is equivalent to either

$$\Delta \log([\text{O III}]/\text{H}\beta)_{\text{S2}} = 0.16 \text{ dex or}$$

$$\Delta \log([\text{S II}]/\text{H}\alpha)_{\text{S2}} = 0.36 \text{ dex.}$$

This significant displacement between the subsample loci in the S2-BPT diagram is intriguing because of its implications for the physical origin of the offset in the N2-BPT plane. Assuming the offset between the small-offset and large-offset subsamples in the N2-BPT plane is entirely a horizontal displacement toward higher $\log([\text{N II}]/\text{H}\alpha)$ resulting from an

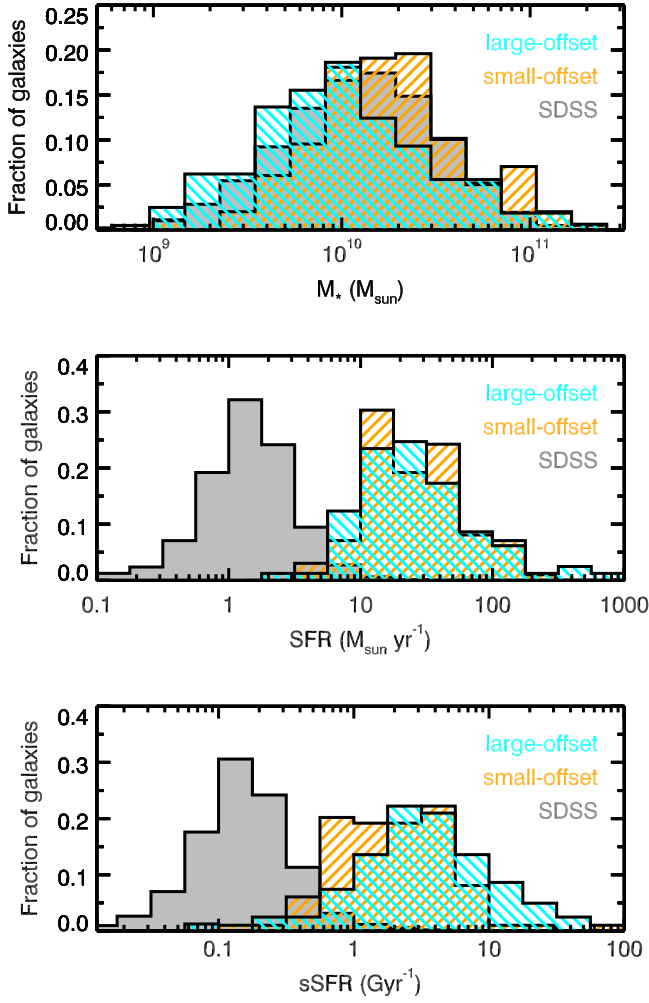


Figure 10. The distributions of M_* , SFR, and sSFR for SDSS galaxies (in gray) and the KBSS-MOSFIRE subsamples divided by the degree of their N2-BPT offset. Although the two $z \sim 2.3$ subsamples have very similar distributions in SFR, they exhibit clear differences in M_* and sSFR. All KBSS-MOSFIRE galaxies have substantially higher SFRs and sSFRs than SDSS galaxies.

enhancement in N/O at fixed O/H implies $\Delta \log([\text{O III}]/\text{H}\beta) \approx 0$. Provided all other abundance ratios (particularly S/O) are similar between small- and large-offset galaxies, $\Delta \log([\text{S II}]/\text{H}\alpha)$ should also be close to zero. The assumption of similar S/O abundances among the two subsamples is reasonable, as sulfur and oxygen are both alpha process elements released primarily by Type II SNe.

Consequently, the two ridge-lines in the right panel of Figure 9 ought to lie coincident with one another if the offset between the subsamples was due primarily to differences in N/O at fixed O/H. Indeed, when Sanders et al. (2016) performed the same exercise using galaxies from the MOSDEF survey, they found that high- z galaxies separated on the basis of their offset from local galaxies in the N2-BPT diagram are well-mixed in the S2-BPT and O32-R23 planes. The authors interpret this result as evidence in favor of elevated N/O at fixed O/H in $z \sim 2.3$ galaxies, but such an explanation is inconsistent with the results shown for the KBSS-MOSFIRE subsamples in Figure 9.

While some horizontal separation between the KBSS-MOSFIRE S2-BPT loci might occur if a larger amount of [S II] emission originated from diffuse ionized gas in large-offset galaxies than in small-offset galaxies, the contribution

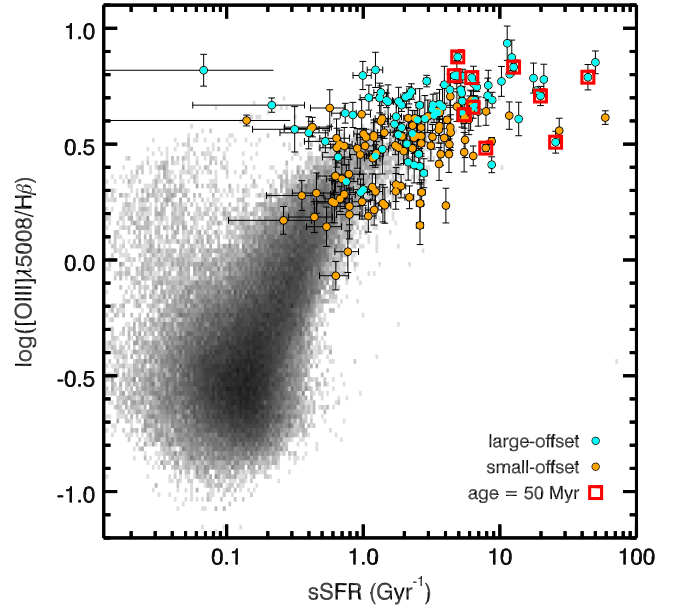


Figure 11. The sSFR-excitation relation for SDSS (in grayscale) and KBSS-MOSFIRE galaxies, with the $z \sim 2.3$ galaxies color-coded by the degree of their N2-BPT offset (large-offset galaxies in cyan, small-offset galaxies in orange; see the left panel of Figure 9). KBSS-MOSFIRE galaxies with an imposed minimum age of 50 Myr from SED fitting are identified by red squares; this sample of galaxies is discussed at greater length in Section 4.3 and Figures 12 and 13. All of the KBSS-MOSFIRE galaxies overlap only with SDSS galaxies with the highest $\log([\text{O III}]/\text{H}\beta)$ and sSFR. However, both $z \sim 2.3$ and $z \sim 0$ samples appear to form a single excitation sequence.

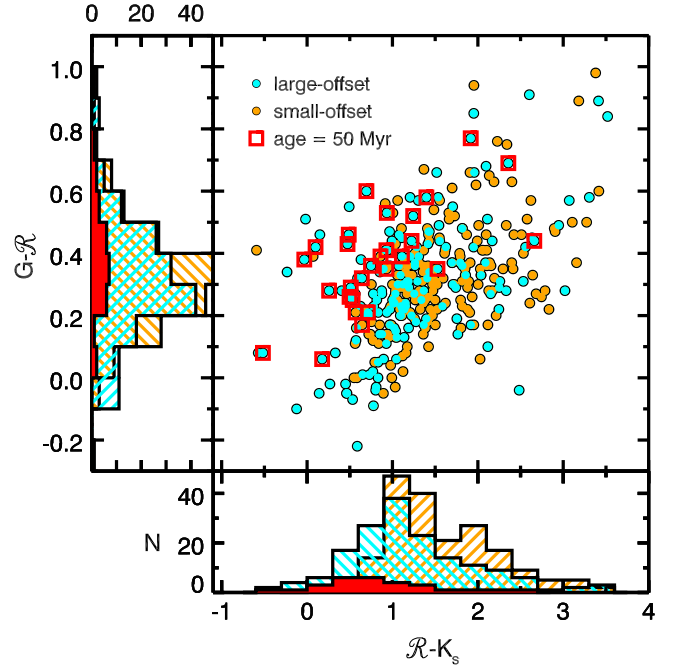


Figure 12. The distribution of $\mathcal{R} - K_s$ and $G - \mathcal{R}$ color for the two subsamples of KBSS galaxies, flanked by 1D histograms to highlight the differences. The large-offset galaxies (cyan) have generally bluer colors than their small-offset counterparts (orange), with fewer small-offset galaxies exhibiting blue optical-NIR colors ($\mathcal{R} - K_s \leq 1$). Galaxies with an imposed minimum age of 50 Myr (which are identified by red squares and are among the quartile of galaxies most offset from the $z \sim 0$ locus) have the bluest $\mathcal{R} - K_s$ colors, which suggests that the maturity of the stellar population is inversely correlated with the degree of offset from SDSS galaxies in the N2-BPT diagram.

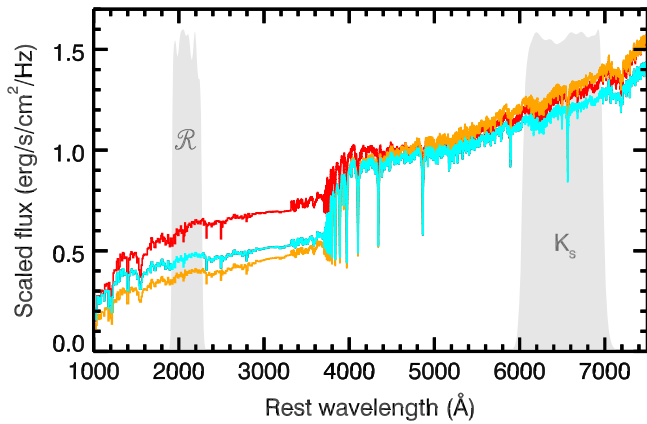


Figure 13. Typical SEDs for subsamples of KBSS-MOSFIRE galaxies (small-offset galaxies in orange, large-offset galaxies in cyan, and minimum-age galaxies in red), showing how differences in global spectral shape correlate with the degree of offset in the N2-BPT plane.

from such gas would need to be substantial to account for the 0.36 dex difference in $\log([\text{S II}]/\text{H}\alpha)$ at fixed $\log([\text{O III}]/\text{H}\beta)$ between the subsamples. Instead, it is likely that the clear separation between the two loci corresponds to important differences in the shape and/or normalization of the ionizing radiation in small- and large-offset galaxies, and similar differences may be important between $z \sim 0$ and $z \sim 2.3$ galaxies. In Section 5.3 we test whether such differences can account for the entirety of the offset observed between KBSS-MOSFIRE and SDSS in the N2-BPT diagram.

4.2. Galaxy Properties

We can also compare the global properties of galaxies as a function of their N2-BPT offset. In general, large-offset galaxies have significantly lower M_* than small-offset galaxies, despite having nearly identical distributions in SFR (see Figure 10). The separation as a function of M_* is consistent with the results reported by Shapley et al. (2015) for $z \sim 2$ MOSDEF galaxies, but the resulting separation in sSFR for KBSS-MOSFIRE galaxies is especially notable. This difference highlights the fact that recent star formation has contributed a larger fraction of the integrated stellar mass of large-offset galaxies than for small-offset galaxies. For comparison, the distributions of M_* , SFR, and sSFR for the SDSS galaxies are shown in gray in Figure 10. Interestingly, the SDSS, small-offset KBSS-MOSFIRE, and large-offset KBSS-MOSFIRE samples appear to form a sequence in sSFR that mirrors their separation in N2-BPT diagram (from least to most offset).

The importance of recent star formation is also apparent in the behavior of $[\text{O III}]/\text{H}\beta$ —which we have already shown is significantly higher for KBSS-MOSFIRE galaxies compared with SDSS and serves as a measure of excitation—as a function of sSFR, which is shown in Figure 11. Unlike M_* -excitation space (Figure 7), KBSS-MOSFIRE galaxies appear to follow the sSFR-excitation trend established by local galaxies in SDSS, with large-offset galaxies exhibiting the highest sSFRs and ratios of $[\text{O III}]/\text{H}\beta$. Dickey et al. (2016) found the same trend for a sample of $z \sim 2$ star-forming galaxies from the 3D-HST survey.

The interquartile range in M_* for SDSS galaxies with $\text{sSFR} > 2 \text{ Gyr}^{-1}$ ($\sim 1\%$ of the total sample) is $\log(M_*/M_\odot) = 8.40\text{--}9.06$, while high sSFRs are found in

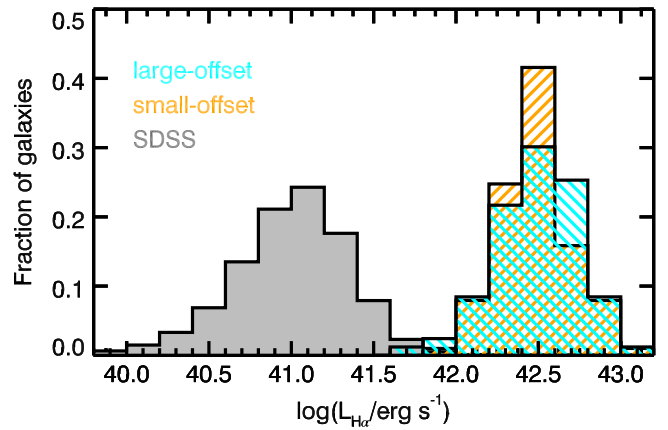


Figure 14. Histograms of $\text{H}\alpha$ luminosity for SDSS galaxies and KBSS-MOSFIRE galaxies, divided on the basis of their N2-BPT offset into large- and small-offset subsamples. Although a Balmer luminosity selection in SDSS mimics the N2-BPT offset observed for $z \sim 2.3$ galaxies, the same behavior is not observed for KBSS-MOSFIRE galaxies, with the two samples having statistically consistent distributions.

significantly more massive $z \sim 2.3$ galaxies. KBSS-MOSFIRE galaxies with $\text{sSFR} > 2 \text{ Gyr}^{-1}$ represent $\sim 57\%$ of the $z \sim 2.3$ sample and are ~ 10 times more massive than high-sSFR $z \sim 0$ SDSS galaxies on average, with an interquartile range in $\log(M_*/M_\odot) = 9.59\text{--}10.11$. If the offset of the two $z \sim 2.3$ subsamples with respect to one another (and with respect to $z \sim 0$) is tied to sSFR, the implication is that the physical cause of the observed differences between samples is also correlated with the relative importance of recent star formation in galaxies at fixed M_* . This highlights the importance of the details of star formation history generally, as the high sSFRs seen in KBSS-MOSFIRE galaxies become increasingly difficult to sustain in older, massive galaxies and/or galaxies that have begun to deplete their gas supply. Consequently, galaxies with the most extreme sSFRs are likely to have rising star formation histories or intense bursts of recent star formation, conditions that are seemingly commonplace at $z \simeq 2\text{--}2.7$ (e.g., Reddy et al. 2012) but rare in the local universe.

4.3. SED Shapes

The KBSS-MOSFIRE subsamples also exhibit significant differences in the characteristic shape of their SEDs, with a larger fraction ($\sim 40\%$) of large-offset galaxies appearing blue in the rest-optical ($(\mathcal{R} - K_s)_{\text{AB}} \leq 1$) than small-offset galaxies ($\sim 19\%$). Figure 12 presents the distributions of both $\mathcal{R} - K_s$ and $G - \mathcal{R}$ color for the two subsamples. Despite a statistically significant difference in $\mathcal{R} - K_s$, the $G - \mathcal{R}$ distributions are nearly identical.

Because $\mathcal{R} - K_s$ color probes the depth of the Balmer and 4000 Å breaks, it traces both age and stellar mass (e.g., Shapley et al. 2005), which is part of the motivation for the RK selection described in Section 2.1. The bluer colors of the large-offset galaxies are therefore consistent with their smaller overall M_* (Figure 10). Additionally, although age estimates from SED fitting are not very robust in an absolute sense, 15% of large-offset galaxies have SEDs that are best fit by a constant star formation history with an age of 50 Myr, compared to only 3% of small-offset galaxies. As discussed in Section 2.5, this age is a minimum imposed to avoid unrealistically young inferred ages. In total, 17/28 (61%) “minimum-age” galaxies (identified by red squares in Figures 11 and 12) fall above even

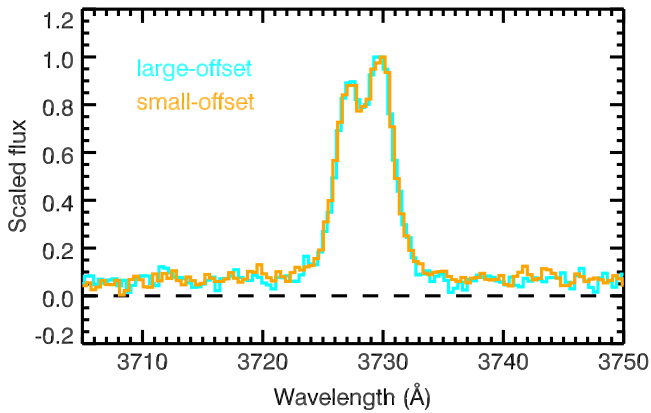


Figure 15. The $[\text{O II}]\lambda\lambda 3727, 3729$ doublet, commonly used to infer n_e in the emitting gas, as observed in stacks of small- and large-offset KBSS-MOSFIRE galaxies. That the n_e estimates for both composites are consistent with one another (values for each subsample are listed in the text) suggests that electron density—and, by extension, ISM pressure—do not play an important role in determining the location of $z \sim 2.3$ galaxies in the N2-BPT plane.

the large-offset N2-BPT locus (cyan curve in Figure 9) and are therefore among the quartile exhibiting the most dramatic offset with respect to SDSS galaxies.

Figure 13 shows the average SED model for small-offset (orange) and large-offset (cyan) galaxies alongside the SED model characteristic of minimum-age galaxies (red), illustrating both the similarities in shape in the rest-UV and the differences across the Balmer break and at rest-optical wavelengths. The SEDs have been constructed by averaging the reddened high-resolution best-fit stellar population synthesis models from Bruzual & Charlot (2003), after scaling each to match between 4500–4600 Å; the continuum extinction for small- and large-offset galaxies is roughly similar, with $\langle E(B - V) \rangle_{\text{small}} = 0.18$ and $\langle E(B - V) \rangle_{\text{large}} = 0.16$. The templates shown in Figure 13 do not include nebular continuum emission, which will further diminish the stellar Balmer break.

The over-representation of minimum-age systems with blue $\mathcal{R} - K_s$ colors among the most offset galaxies suggests that selection techniques that rely on the presence of a significant Balmer break may not reliably identify such galaxies. Conversely, the fact that small- and large-offset KBSS-MOSFIRE galaxies show no obvious separation in their rest-UV colors—despite differences in their rest-optical colors and nebular emission line properties—suggests that the selection techniques described in Section 2.1 are not strongly biased in favor of large-offset galaxies; in fact, the RK selection described in Section 2.1 will favor galaxies with larger Balmer breaks, like the small-offset galaxies.

4.4. Balmer Emission Line Luminosity

Juneau et al. (2014) showed that a Balmer emission line luminosity selection applied to SDSS galaxies could result in a sample that exhibits an N2-BPT offset of similar magnitude to that reported for $z \sim 2$ galaxies. More recently, Cowie et al. (2016) suggested that Balmer line luminosity may be an efficient way of identifying low-redshift analogs of typical $z \sim 2$ galaxies. Given these results, the magnitude of the N2-BPT offset observed in KBSS-MOSFIRE could be artificially inflated if the sample were biased toward galaxies with the highest Balmer luminosities. It is interesting therefore to

consider whether large-offset galaxies are overrepresented in KBSS-MOSFIRE due to such observational biases.

Figure 14 shows the distribution of observed $H\alpha$ luminosity, uncorrected for dust extinction, for the small- and large-offset KBSS-MOSFIRE subsamples, as well as that for the full SDSS comparison sample. For SDSS galaxies, $L_{H\alpha}$ has been corrected for aperture effects using the ratio of the total inferred SFR to the SFR measured from the fiber. All KBSS-MOSFIRE galaxies exhibit significantly higher line luminosities than typical $z \sim 0$ galaxies, but the $z \sim 2.3$ subsamples are statistically consistent with being drawn from the same parent population as each other ($p = 0.55$ from a two-sample Kolmogorov–Smirnov test). Moreover, when the full KBSS-MOSFIRE sample is divided by $H\alpha$ luminosity, fits to the N2-BPT loci do not show a significant offset with respect to one another in either $\log([\text{O III}]/H\beta)$ or $\log([\text{N II}]/H\alpha)$. Together, these results suggest that observational biases do not significantly impact the degree of the observed N2-BPT offset and that $H\alpha$ luminosity is not strongly correlated with the location of $z \sim 2.3$ galaxies in the N2-BPT plane. In fact, the observing strategy outlined in Section 2.1 mitigates this kind of incompleteness, as observations of individual galaxies are repeated until the strongest lines (including $H\alpha$) are significantly detected.

4.5. Electron Density

Finally, we consider differences between the large- and small-offset samples in terms of the electron density (n_e) in their H II regions. Sanders et al. (2016) offered a thorough discussion of electron density estimates for $z \sim 2$ star-forming galaxies using observations from the MOSDEF survey, noting that electron densities inferred from both the $[\text{O II}]\lambda\lambda 3727, 3729$ and $[\text{S II}]\lambda\lambda 6718, 6732$ doublets are an order of magnitude higher for $z \sim 2$ galaxies in their sample relative to a comparison sample from SDSS. At the same time, a number of studies have demonstrated that galaxies with higher electron densities ($n_e \sim 10^2 \text{ cm}^{-3}$) exhibit higher $\log([\text{N II}]/H\alpha)$ and $\log([\text{O III}]/H\beta)$ than typical SDSS galaxies (e.g., Brinchmann et al. 2008; Liu et al. 2008; Yuan et al. 2010), often associated with higher inferred ionization parameters and differences in ISM pressure (Lehnert et al. 2009; Kewley et al. 2013). One may therefore expect large-offset KBSS-MOSFIRE galaxies to exhibit higher electron densities than small-offset galaxies.

To estimate n_e for the KBSS-MOSFIRE subsamples, we rely on inferences from spectral stacks, in order to consistently account for individual galaxies with lower S/N observations of the density-sensitive $[\text{O II}]$ doublet. Galaxies from the small- and large-offset subsamples were corrected for slit losses and then averaged separately, masking regions contaminated by OH emission lines. The spectral region near the $[\text{O II}]$ doublet is shown in Figure 15, where the J band stacks have been scaled by the peak flux in the $[\text{O II}]\lambda 3729$ line for ease of comparison.

For the small-offset composite, $I(3729)/I(3727) = 1.13 \pm 0.03$, and for the large-offset composite, $I(3729)/I(3727) = 1.14 \pm 0.04$. Using the diagnostic relation from Sanders et al. (2016), which assumes $T_e = 10^4 \text{ K}$, these values correspond to

$$n_{e,\text{small}} = 281_{-39}^{+43} \text{ cm}^{-3}$$

$$n_{e,\text{large}} = 267_{-43}^{+48} \text{ cm}^{-3}.$$

These values are consistent with one another within measurement uncertainties and also with the median value reported by Sanders et al. (2016) for MOSDEF galaxies using the [O II] diagnostic ($n_{e,\text{MOSDEF}} = 225 \text{ cm}^{-3}$).

The similarity between the electron density estimates for the two KBSS-MOSFIRE subsamples suggests that n_e is not strongly correlated with the physical process(es) that determine the position of $z \sim 2.3$ galaxies in the N2-BPT diagram, in contrast to observations of galaxies in the local universe.

5. Nitrogen-to-oxygen Abundance Ratios

Nitrogen is formed as part of the CNO cycle in intermediate mass and massive stars, both as a primary and secondary element. Primary nitrogen production is regulated by the C, N, and O created within stars formed out of relatively metal-poor gas, whereas secondary production is seeded by the C, N, and O initially present in stars (as the result of prior enrichment of the ISM). This double nature is reflected by the well-documented behavior of the N/O abundance ratio as a function of O/H for samples of galaxies and H II regions (e.g., Diaz & Tosi 1986; van Zee et al. 1998), where N/O remains at a constant value ($\log(\text{N/O}) \approx -1.5$) for low values of $12+\log(\text{O/H})$ ($\lesssim 8.0$) but rapidly increases with increasing oxygen abundance at higher values of O/H.

The precise relationship between N/O and O/H is a matter of some debate in the literature, depending sensitively on the choice of sample and method of measurement, making it difficult to place the N/O reported for individual sources or small samples in context. At $z \sim 0$, many studies rely on measurements from the spectra of individual compact galaxies or local H II regions (e.g., Pérez-Montero & Contini 2009; Pilyugin et al. 2012) or from composite spectra of relatively metal-poor galaxies (Andrews & Martini 2013), but the typical value of N/O at a given measured value of O/H can vary by up to 0.5 dex. As we discussed in S14, the differences between such studies may be dominated by differences in the method used to measure O/H. It has been argued separately that scatter in the N/O–O/H relation is due instead to the effects of pristine gas inflow (e.g., Köppen & Hensler 2005), which could lower O/H while leaving N/O largely unaffected, particularly if much of the nitrogen is formed in intermediate mass stars that take longer to return their nucleosynthetic products to the ISM.

In Section 4.1, we briefly addressed the idea that the N2-BPT offset observed for $z \sim 2.3$ galaxies could be due primarily to an enhancement in N/O relative to typical local galaxies with the same gas-phase oxygen abundance (as proposed by, e.g., Masters et al. 2014, 2016; Shapley et al. 2015; Cowie et al. 2016; Sanders et al. 2016). If found to be present in high-redshift galaxies, such systematic deviations in N/O would have serious implications for calibrations linking nebular emission line ratios that include nitrogen lines (e.g., [N II] $\lambda 6585$) to oxygen abundance. Strong-line abundance calibrations rely on the implicit assumption that N/O varies similarly with O/H for both the calibration sample and the objects of interest, and many photoionization models likewise impose a prior on the value of N/O expected at a given O/H.

From an astrophysical perspective, it is also a concern that there is presently no consensus regarding the physical process(es) that might result in enhanced N/O for the majority of high-redshift galaxies. Although Masters et al. (2014) favored the existence of a large population of Wolf–Rayet stars as one possible explanation, the lifetimes of such stars are short,

meaning that the effect would be limited to systems with extremely young ages (as discussed by Shapley et al. 2015). More recently, Masters et al. (2016) have suggested that the existence of a redshift invariant or slowly evolving N/O– M_* relation, when combined with the strong evolution toward lower O/H at fixed M_* observed at $z > 1$ (e.g., Erb et al. 2006a; Steidel et al. 2014; Wuyts et al. 2014; Sanders et al. 2015), might more plausibly explain a systematic increase in N/O at fixed O/H for high-redshift galaxies.

The Masters et al. (2016) study relied on a detailed analysis of $\sim 100,000$ star-forming galaxies from SDSS-DR12 and compared the behavior of $z \sim 0$ galaxies with the results from stacked spectra from the FMOS-COSMOS survey at $z \sim 1.6$ reported by Kashino et al. (2016). However, to fairly evaluate the likelihood of the proposed explanations, observations of a statistical sample of individual $z \sim 2$ galaxies are necessary. In this section, we present the first efforts to explicitly examine N/O for such a sample, using observations of the $z \sim 2.3$ KBSS-MOSFIRE sample to investigate the behavior of N/O as a function of other measured galaxy properties.

5.1. Strong-line Abundance Calibration Using N2O2

For ionized gas, the most reliable measurements of O/H and N/H—and thus N/O—are derived from the measurement of electron temperature (T_e), which is often described as the “direct” method. Unfortunately, these measurements are extremely challenging, even for galaxies in the local universe, as the auroral emission lines necessary for measuring T_e of both singly and doubly ionized species are relatively weak compared to their nebular counterparts and become more difficult to measure for objects with increasing gas-phase abundance. The situation is even worse for distant objects, including star-forming galaxies at high redshift.

The most practical alternative is to rely on strong-line indices known to exhibit tight correlations with intrinsic O/H and N/O. For oxygen abundance, two of the most widely used indices are N2 and O3N2 (Table 3). For N/O, N2O2 and N2S2 (also defined in Table 3) are the most common choices. One of the most serious outstanding challenges to using strong-line calibrations for these indices is knowing whether or not they are reliable for sources that differ from those used to establish the original calibration between emission line ratio and metallicity. The existence of the strong N2-BPT offset cautions against the application of locally calibrated relations for N2 and O3N2 at high redshift, as they will inevitably return inconsistent estimates of $12+\log(\text{O/H})$ with respect to one another for objects that are offset from the $z \sim 0$ locus. Studies of local objects have also shown that a factor of ~ 2 – 3 enhancement in N/O at fixed O/H (measured using the direct method) is not recovered when both N/O and O/H are estimated using strong-line methods, because O/H is overestimated for such objects (Pilyugin et al. 2010). Furthermore, as we previously discussed in S14, photoionization models suggest that many of the strong-line ratios are more strongly correlated with the details of the ionizing radiation field than gas-phase oxygen abundance, particularly for high-excitation nebulae.

In contrast, the calibration for N/O using N2O2 relies primarily on the assumption that due to the similarity in the ionization potentials for O and N, the relative ionization correction factors are also similar and thus $\log(\text{N/O}) \simeq \log(\text{N}^+/\text{O}^+)$. This makes N2O2 considerably less sensitive to

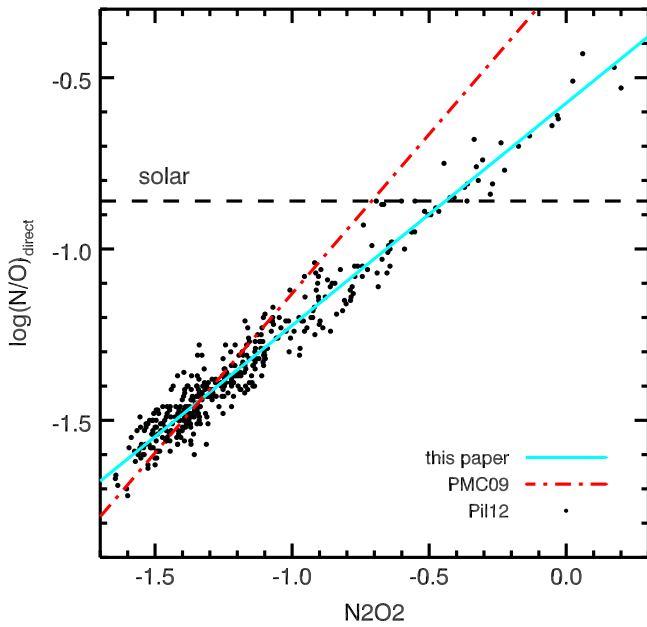


Figure 16. The observed N2O2 index and T_e -based N/O measurements for the extragalactic H II regions from Pilyugin et al. (2012). The best-fit linear relation, which is used in this paper, is shown in cyan. The relation from Pérez-Montero & Contini (2009) is shown by the dashed red line for comparison.

changes in the ionization parameter and/or the shape of the ionizing radiation than O3N2 or N2.

We employ a new calibration for N/O derived using a sample of extragalactic H II regions compiled by Pilyugin et al. (2012, hereafter Pii12). The 414 sources described therein have direct method measurements of both nitrogen and oxygen abundance, as well as measurements of [O II] $\lambda\lambda$ 3727, 3729; H β , [O III] $\lambda\lambda$ 4960, 5008; [N II] $\lambda\lambda$ 6549, 6585; H α ; and [S II] $\lambda\lambda$ 6718, 6732. In most cases, the electron temperature was measured directly for only one ion (and thus only one temperature zone); since the authors adopt a two-zone model, the temperature in the second zone is determined using the relations from Campbell et al. (1986) and Garnett (1992).

Figure 16 shows the N2O2 and N/O measurements for the Pii12 sample and the corresponding calibration used in this paper (in cyan). For reference, the calibration from Pérez-Montero & Contini (2009, PMC09) is shown in red, highlighting the differences that can arise from the choice of calibration sample, particularly when both individual H II regions and entire galaxies are considered, as is the case with Pérez-Montero & Contini (2009). For the new calibration, we have fit to the entire range in N/O, since the spread in observed N2O2 is nearly identical for KBSS-MOSFIRE and the Pii12 sample. The resulting relation is

$$\log(\text{N/O}) = 0.65 \times \text{N2O2} - 0.57, \quad (5)$$

with an accompanying RMS scatter about the best-fit relation of $\sigma_{\text{RMS}} = 0.05$ dex. Adopting the PMC09 calibration instead of Equation (5) would imply values of $\log(\text{N/O})$ larger by up to ~ 0.3 dex.

The use of N2S2 as an alternative to N2O2 presents many practical advantages, as it requires observations in only one NIR band, and thus needs fewer observations, needs no cross-band calibration, and is much less sensitive to relative extinction due to dust. However, the mapping of N2S2 to N/O relies on the expectation that S/O remains constant, and

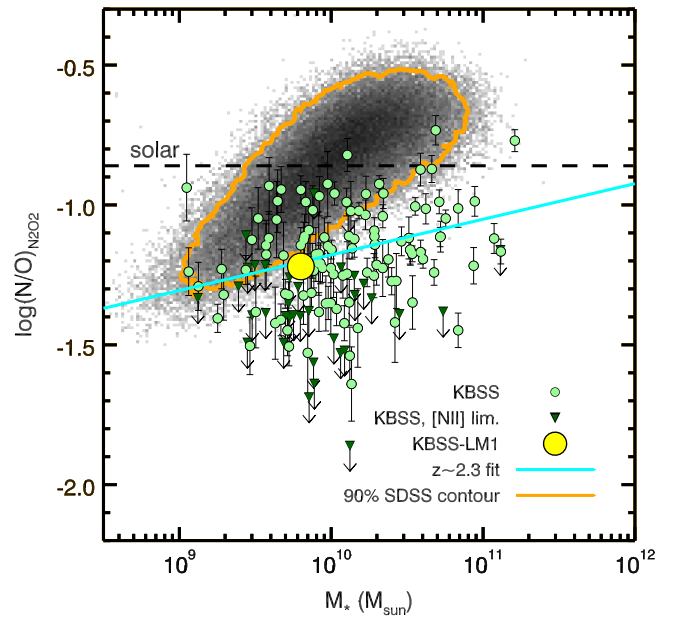


Figure 17. N/O measurements for KBSS-MOSFIRE galaxies (excluding AGN) as a function of M_* , plotted alongside the $z \sim 0$ SDSS sample (with the orange contour enclosing 90% of the local galaxies). KBSS-MOSFIRE galaxies exhibit significantly lower N/O at fixed M_* relative to SDSS galaxies, which show a strong positive correlation between both parameters. The more moderate positive correlation observed for the $z \sim 2.3$ KBSS-MOSFIRE galaxies can be approximated by a linear relation (Equation (6)), which is shown in cyan. The location of the Steidel et al. (2016) composite spectrum in this parameter space is represented by the large yellow point, showing that it is fully consistent with the $z \sim 2.3$ relation.

therefore that sulfur may be used as a proxy for oxygen. Because the ionization potentials of O (13.62 eV) and S (10.4 eV) differ significantly, however, [S II]-emitting gas may not be entirely spatially coincident with the region where the [O II] emission originates, and could lie well outside of the H-ionizing region. Thus, despite the advantages of requiring observations in only one NIR window and no extinction correction, we rely exclusively on the N2O2 index in this paper.

5.2. Correlation with Galaxy Properties

We infer N/O for 151 galaxies in the $z \sim 2.3$ KBSS-MOSFIRE sample using Equation (5). Galaxies were included in the sample if they had a $\geq 3\sigma$ detection of the combined [O II] $\lambda\lambda$ 3726, 3729 doublet and H β , a $\geq 5\sigma$ detection of H α , and a robust measurement of the Balmer decrement (as described in Section 2.5); objects with $< 2\sigma$ detections of [N II] were assigned 2σ upper limits.

Figure 17 shows the N/O- M_* relation for $z \sim 2.3$ KBSS-MOSFIRE galaxies compared with $z \sim 0$ SDSS galaxies. As for local galaxies, the KBSS-MOSFIRE sample exhibits a positive correlation between N/O and M_* (with Spearman correlation coefficient $\rho = 0.24$ and $p = 0.01$). The best-fit linear relation describing the sample is

$$\log(\text{N/O}) = -1.18 + 0.13 \times [\log(M_*/M_\odot) - 10], \quad (6)$$

which has $\sigma_{\text{RMS}} = 0.17$ dex.

The $z \sim 2.3$ locus is noticeably offset relative to typical SDSS galaxies (enclosed by the orange contour) at fixed M_* . At low stellar masses, the difference between the two samples is small, but becomes larger with increasing M_* , reaching an offset of ~ 0.5 dex toward lower $\log(\text{N/O})$ at $M_* \sim 10^{11} M_\odot$; if

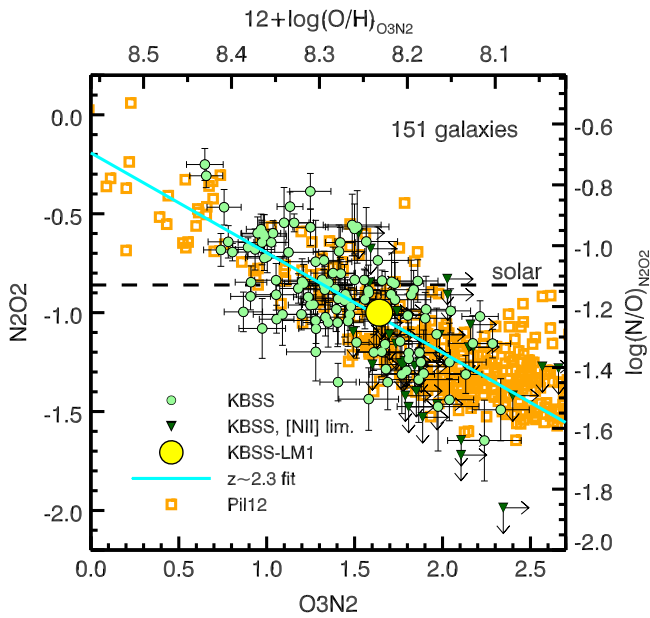


Figure 18. N2O2 as a function of O3N2 for both $z \sim 2.3$ KBSS-MOSFIRE galaxies (green points, with 2σ upper limits in [N II] shown as dark green triangles) and extragalactic H II regions from Pii12 (orange squares). Both samples behave similarly and exhibit comparable degrees of scatter in this observed line ratio space. For comparison, the location of the composite spectrum of KBSS galaxies from S16, which shows no enhancement in N/O at fixed O/H relative to the Pii12 sample, is shown by the large yellow point. The best-fit linear relation for the full KBSS-MOSFIRE sample is shown in cyan; if interpreted as a N/O–O/H relation using $\log(N/O)$ derived from N2O2 (see right axis, Equation (5)) and estimates of $12+\log(O/H)$ from O3N2 (see top axis, Equation (7)), this relation is fully consistent with the T_e -based N/O–O/H relation observed for the Pilyugin et al. (2012) sample.

the $z \sim 0$ locus is also approximated by a linear relation, the average separation between 10^9 and $10^{11} M_\odot$ is ~ 0.32 dex in $\log(N/O)$. This is a much larger shift than that observed (albeit using N2S2) for the $z \sim 1.6$ FMOS-COSMOS stacks from Kashino et al. (2016). Moreover, those authors reported the largest differences relative to SDSS at low stellar masses ($M_* \sim 10^{9.5}$), the opposite of the trend seen here for KBSS-MOSFIRE galaxies.

Clearly, the N/O– M_* relation evolves significantly between $z \sim 0$ and $z \sim 2.3$. However, high- z galaxies would still exhibit higher values of N/O at fixed O/H relative to $z \sim 0$ galaxies if the N/O– M_* relation evolves more slowly than the O/H M_* -metallicity relation (MZR). Although it remains difficult to measure O/H independently of N for many individual high- z galaxies, there is some evidence to suggest that the redshift evolution of the N/O– M_* relation and the MZR are comparable: S14 showed that oxygen abundances measured using the O3N2 index exhibit the least bias and scatter relative to the direct method for individual KBSS-MOSFIRE galaxies with T_e -based measurements, and that when O3N2 is used to estimate O/H, $z \sim 2.3$ galaxies exhibit a 0.32 dex offset toward lower $12+\log(O/H)$ at fixed M_* relative to SDSS. Furthermore, in S16, we reported a direct, T_e -based O/H abundance for a stack of KBSS galaxies and N/O independently inferred using both photoionization modeling and the strong-line calibration from Equation (5) of this paper. These measurements show that the KBSS stack, which is representative of the full KBSS-MOSFIRE sample discussed here (cf. the yellow point in Figure 17), is consistent with the

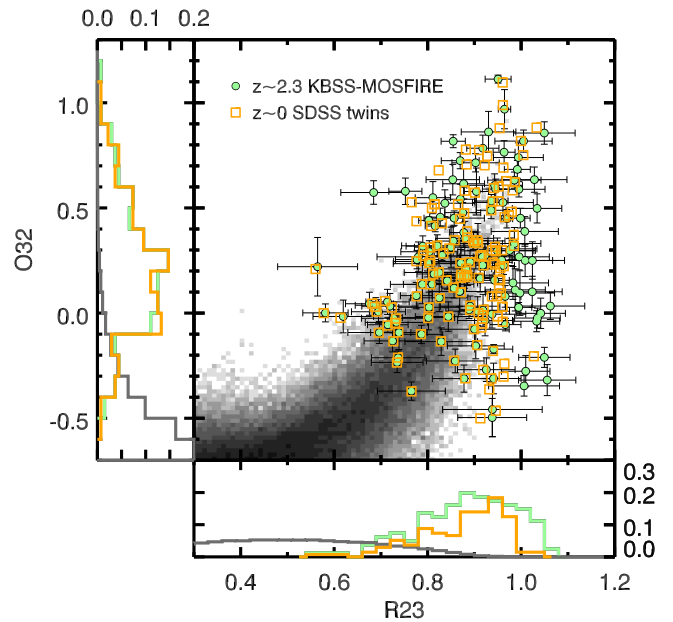


Figure 19. The distribution of $z \sim 2.3$ KBSS-MOSFIRE galaxies and $z \sim 0$ SDSS twins in the O32-R23 plane. Each SDSS comparison galaxy (shown by the open orange squares) is chosen based on proximity to a KBSS-MOSFIRE galaxy (represented by the green points with error bars) in both parameters. This selection technique ensures that the distributions of R23 and O32 are statistically consistent for the two samples, as can be seen in the flanking histograms of both line ratios. For comparison, the distributions of O32 and R23 for the full SDSS sample are shown in gray.

N/O–O/H relation observed for the sample of H II regions from Pii12 (see Figure 16 of Steidel et al. 2016).

Taken together, these results suggest that the N/O–O/H relation is redshift invariant. Confirming the universality of the N/O–O/H relation must await independent measurements of N/O and O/H for a large sample, and we discuss the possibility of obtaining such measurements for KBSS-MOSFIRE galaxies in Section 6.3. For now, we consider the behavior of N2O2 as a function of O3N2 for the KBSS-MOSFIRE galaxies (green) and the Pii12 sample (orange) in Figure 18. The best-fit linear relation describing the KBSS-MOSFIRE locus (cyan line) also traces the behavior of the Pii12 sample in terms of observed line ratios. Indeed, there is virtually no separation in either N2O2 or O3N2 between the samples, except for $O3N2 > 2.5$, where there are no KBSS-MOSFIRE galaxies. The reason for the lack of $z \sim 2.3$ galaxies in that region of parameter space is easily understood as a selection effect in the KBSS-MOSFIRE sample; high values of O3N2 correspond to low values of $12+\log(O/H)$, and at such low metallicities, the strength of both oxygen and nitrogen emission lines begins to decline below practical detection limits.

We can establish a calibration mapping O/H to O3N2 for the Pii12 sample, as we did for N/O and N2O2 in Section 5.1, resulting in the following linear relation⁹:

$$12 + \log(O/H) = 8.56 - 0.20 \times O3N2; \quad \sigma_{\text{RMS}} = 0.08 \text{ dex.} \quad (7)$$

Such a calibration will disguise a potential enhancement in N/O at fixed O/H, but if we assume that the N/O–O/H relation is indeed the same at all redshifts, the linear fit to the

⁹ We include only H II regions with $12+\log(O/H) > 8.0$ in determining the calibration.

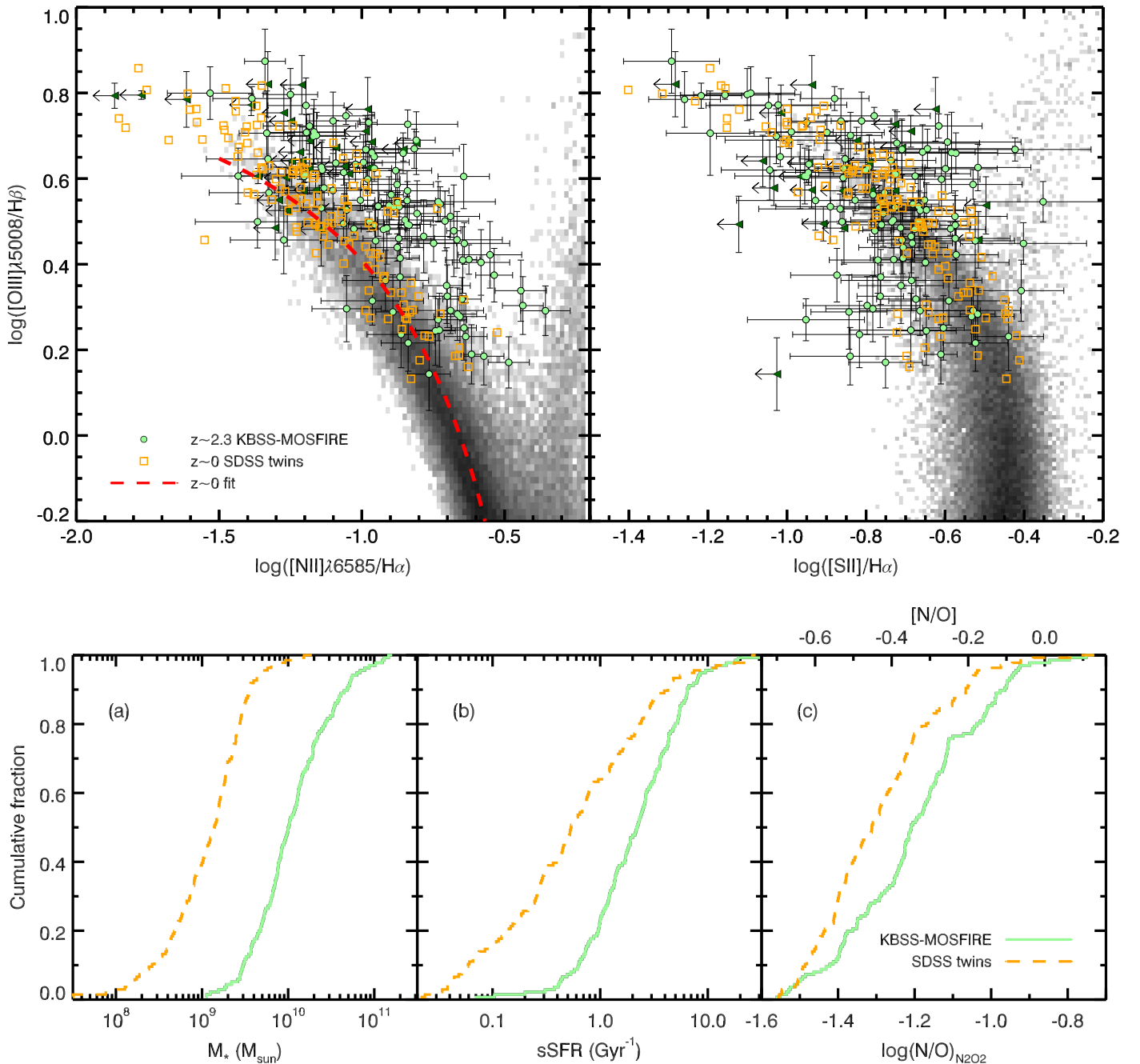


Figure 20. A comparison of the nebular, physical, and chemical properties of $z \sim 2.3$ KBSS-MOSFIRE galaxies and their $z \sim 0$ SDSS twins matched in O32 and R23, as described in the text and shown in Figure 19. The upper row illustrates the differences in the N2- and S2-BPT diagrams, which are consistent with the results described in Section 3.1. In the N2-BPT plane there is a strong offset observed between KBSS-MOSFIRE galaxies (green points with error bars, 2σ upper limits in [N II] drawn as dark green triangles) and the SDSS twins (open orange squares), with no significant separation in the S2-BPT plane (here the dark green triangles represent 2σ upper limits in [S II]). The bottom panels show differences in the physical properties of KBSS-MOSFIRE galaxies (solid green curves) and SDSS twins (dashed orange curves; from left to right: M_* , sSFR, and N/O determined from N2O2 (Equation (5))). The ~ 0.10 dex higher values of $\log(\text{N/O})$ observed in KBSS-MOSFIRE galaxies fall short of accounting for the horizontal displacement of $z \sim 2.3$ galaxies relative to SDSS in Figure 5 and are much lower than would be expected if the N/O- M_* relation were redshift invariant.

$z \sim 2.3$ KBSS-MOSFIRE locus in Figure 18 can then be described as

$$\log(\text{N/O}) = -1.29 + 1.64 \times [(12 + \log(\text{O/H})_{\text{O3N2}}) - 8.2]. \quad (8)$$

This relation is slightly steeper but statistically consistent with a linear relation determined using only T_e -based measurements of N/O and O/H for the Pil12 sample. Because of this

similarity, we use Equation (8) in Section 6.2, but note that the results presented there would be the same if we used a fit to the T_e -based measurements from Pil12.

5.3. N/O at Fixed Ionization and Excitation

We have already discussed the likelihood that SDSS galaxies occupying the same region of parameter space in the O32-R23 plane possess similar ionization and excitation properties as

neighboring KBSS-MOSFIRE galaxies. This claim was based on the nature of the O32 and R23 indices; sources with maximal R23 are expected to have similar (moderate) oxygen abundances, so that O32 independently tracks ionization parameter, with higher values of O32 corresponding to higher degrees of ionization. The value of R23 at fixed U and O/H is likewise set by the shape of the ionizing spectrum, as we reasoned in Section 3.4 and show explicitly in Section 6.

However, given the obvious discrepancy between typical values of O32 and R23 for $z \sim 0$ and $z \sim 2.3$ galaxies (Figure 8) and the similarly dramatic separation in $[\text{O III}]/\text{H}\beta$ (Figures 7 and 11), it is necessary to test whether differences in the shape and normalization of the ionizing spectrum account for all (or most) of the differences observed between the nebular properties of $z \sim 0$ and $z \sim 2.3$ galaxies, including the N2-BPT offset. To make a fair comparison between KBSS-MOSFIRE and SDSS, it is imperative to select a sample of SDSS galaxies in a way that matches the high-redshift distribution of these quantities. Because high-ionization, high-excitation galaxies are common at $z \sim 2.3$ yet relatively rare at $z \sim 0$, imposing a simple cut in both line ratios will sample only the tail of local galaxies and lead to significantly different distributions in O32 and R23 (and thus ionization and excitation) for the low- and high-redshift samples.

Instead, we identify an SDSS “twin” for each of the 150 $z \sim 2.3$ KBSS-MOSFIRE galaxies with $>5\sigma$ measurements of $\text{H}\alpha$, $>3\sigma$ measurements of $\text{H}\beta$, $[\text{O III}]$ and $[\text{O II}]$, and $>5\sigma$ significance measurements of the Balmer decrement (see Figure 19). For each KBSS-MOSFIRE galaxy (identified by green points with error bars), the closest SDSS galaxy in the O32-R23 diagram within 2σ measurement uncertainties is selected (represented by open orange squares). To ensure a unique comparison sample, the next closest SDSS galaxy is chosen in cases where a single SDSS galaxy is the closest “twin” for more than one KBSS-MOSFIRE galaxy. There are 17 KBSS-MOSFIRE galaxies without an SDSS galaxy within 2σ measurement uncertainties, due largely to the absence of SDSS galaxies with very large values of R23 at fixed O32. KBSS-MOSFIRE galaxies without SDSS twins were removed from the sample described here and excluded from the analysis in this section. The resulting distributions of O32 and R23 for the KBSS-MOSFIRE sample and the SDSS twins are shown in the flanking panels of Figure 19 and are statistically consistent with being drawn from the same parent distributions of these quantities. For comparison, the distributions of O32 and R23 for the full SDSS sample are shown in gray.

We consider the nebular and chemical properties of KBSS-MOSFIRE galaxies and the SDSS twins in Figure 20. The upper panels show the distribution of both samples in the N2-BPT and S2-BPT planes. Even for galaxies matched in O32 and R23, there is a large offset between the KBSS-MOSFIRE galaxies and their SDSS twins in the N2-BPT plane, whereas there is no apparent separation in the S2-BPT plane, consistent with the behavior observed for the full samples of $z \sim 0$ and $z \sim 2.3$ galaxies presented in Section 3.1. Notably, the SDSS twins fall largely above the ridge-line of the full SDSS sample (red dashed line), such that the offset between the orange squares and green points in the upper left panel of Figure 20 is almost entirely horizontal. The median horizontal offset of KBSS-MOSFIRE galaxies relative to their SDSS twins is equivalent to a 0.18 dex shift toward higher $\log([\text{N II}]/\text{H}\alpha)$, whereas the median $\Delta \log[\text{O III}]/\text{H}\beta < 0.01$ dex. This result is

largely in agreement with Shapley et al. (2015), who reported an offset in the N2-BPT plane for low-mass ($M_* < 10^{10.11} M_\odot$) MOSDEF galaxies relative to SDSS galaxies matched in O32 and R23. Contrary to the MOSDEF results, however, both low- and high-mass KBSS-MOSFIRE galaxies are offset with respect to their SDSS twins, with median offsets in $\log([\text{N II}]/\text{H}\alpha)$ of 0.17 dex for $M_* < 10^{10.11} M_\odot$ and 0.19 dex for $M_* \geq 10^{10.11} M_\odot$.

KBSS-MOSFIRE galaxies are also ~ 10 times more massive than SDSS galaxies matched in O32 and R23 (see panel (a) in the bottom row of Figure 20). While SDSS twins have higher sSFRs than the majority of SDSS galaxies (Figure 10), panel (b) shows that KBSS-MOSFIRE galaxies still have 0.58 dex higher sSFRs on average. Panel (c) in the bottom row of Figure 20 presents the distribution of N/O for both samples, showing that the $z \sim 2.3$ KBSS-MOSFIRE galaxies have higher N/O than their SDSS twins ($p = 1.1 \times 10^{-5}$ that they are drawn from the same distribution), with a median difference of 0.10 dex. These results are broadly consistent with the trends observed for all SDSS galaxies (Masters et al. 2016); however, based on the difference in M_* observed between KBSS-MOSFIRE galaxies and the SDSS twins, the $z \sim 2.3$ galaxies should exhibit N/O close to solar ($\log(\text{N/O}) = -0.86$, $[\text{N/O}] = 0.0$) if the N/O- M_* is redshift invariant, as the authors propose. Additionally, the observed difference in N/O falls markedly short of the 0.37 dex enhancement in N/O that would be required to explain the separation between the $z \sim 0$ and $z \sim 2.3$ N2-BPT loci in Figure 5 if the difference were entirely in $\log([\text{N II}]/\text{H}\alpha)$.

Although we do not report O/H measurements for individual KBSS-MOSFIRE galaxies here, we note that 0.10 dex higher N/O would correspond to only a 0.06 dex difference in O/H if $z \sim 2.3$ galaxies follow the N/O-O/H relation in Equation (8). As we will show in the next section, such a difference in O/H would not be readily apparent in S2-BPT and O32-R23 diagnostic diagrams, as those nebular line ratios are relatively insensitive to changes in O/H in high-excitation nebulae, particularly at moderate gas-phase metallicities.

6. Photoionization Models

Many inferences regarding the properties of high- z H II regions can be made by comparing observations of their nebular spectra with carefully chosen samples of analogous objects, usually low-redshift sources whose characteristic physical conditions are more easily established due to the availability of higher S/N data and/or large sample sizes; we employed this technique in Section 5 to infer the distribution of N/O in the $z \sim 2.3$ KBSS-MOSFIRE sample. Still there remain limitations to using calibrations based on comparison samples that may differ systematically in some key parameter—including the inability to construct suitable calibrations for characteristics that depend on several correlated variables, like the ionization parameter (U).

Photoionization models predict the nebular spectrum produced by a specific combination of input ionizing spectrum, ionization parameter, chemical abundance pattern, and physical conditions in the emitting gas (e.g., electron density). A common shortcoming of photoionization model comparisons, however, is that the large number of free parameters makes it difficult to infer physically meaningful results from the agreement between a given model grid and the data. Ideally, some of the inputs to the photoionization model can be fixed

using independent measurements, leaving only a small number of parameters to vary; in this case, the agreement between a specific set of photoionization models and the data constrains the allowed range of those parameters.

One of the strengths of conducting a survey of $z \simeq 2\text{--}3$ galaxies is the ability to simultaneously obtain spectra in the rest-UV and rest-optical wavebands. Together, observations of both spectral windows provide probes of the massive stars and the surrounding gas that is being ionized and heated by radiation from the same stars. In S16 we described the results from a campaign of deep rest-UV spectroscopic follow-up of KBSS galaxies with MOSFIRE spectroscopy, specifically focusing on demonstrating the ability to account simultaneously for the observed stellar FUV spectrum and the UV-optical nebular spectrum using a set of physically motivated photoionization models. The models used here represent a small subset of those described in that paper, where we discussed them in detail; for completeness, we briefly summarize the salient features.

We use Cloudy (v13.02, Ferland et al. 2013) to predict the nebular spectrum of the irradiated gas given an incident radiation field with a fixed spectral shape. The models assume a plane-parallel geometry where the intensity of the radiation field is parameterized by the ionization parameter $U (\equiv n_\gamma/n_H)$. For ionized gas, n_H is roughly equivalent to the electron density (n_e) and is assumed to be 300 cm^{-3} based on measurements of the density-sensitive [O II] and [S II] doublets from the rest-optical composite spectrum of 30 KBSS-MOSFIRE galaxies (S16). This value is also consistent with the densities reported in S14 for an early sample of KBSS-MOSFIRE galaxies and with the stacked spectra of the small-offset and large-offset subsamples presented in Section 4.5. Because n_H is fixed, U may be interpreted as the normalization of the ionizing radiation field.

Our earlier work (S14) relied on similar models, but eschewed a specific choice of spectral synthesis model, instead using blackbodies to parameterize the shape of the input ionizing spectrum. Here we employ stellar population models from the most recent version of “Binary Population and Spectral Synthesis” (BPASSv2; J. J. Eldridge et al. 2017, in preparation; Stanway et al. 2016). The most important aspect of BPASSv2 relative to other stellar population synthesis codes is the inclusion of interacting massive binary stars, which has the net effect of boosting the overall ionizing flux and producing a significantly harder ionizing spectrum for models with continuous star formation histories, particularly at low stellar metallicity. We adopt the default IMF for BPASSv2, with an IMF slope of -2.35 over the range $0.5 \leq M_*/M_\odot \leq 300$.¹⁰

The metallicity of the gas (Z_{neb}) is allowed to vary independently and is not required to match the stellar metallicity (Z_*) of the input population synthesis model, where Z_* is the fraction of metals by mass and $Z_\odot = 0.0142$ (Asplund et al. 2009). Although the metallicity of the gas near young, massive stars should closely trace the stellar metallicity, decoupling Z_{neb} from Z_* reflects the understanding that high-redshift galaxies may not exhibit solar abundance ratios, particularly between elements synthesized by stars of different masses (as is the case for O/Fe). We specifically highlight O/Fe because the cooling of hot, ionized gas (and thus many features in the nebular spectrum) is regulated largely by the

abundance of O, whereas the shape of the ionizing spectrum is instead determined by the abundance of Fe, which accounts for much of the total opacity in stellar atmospheres and, in turn, governs mass loss rates. As we discussed in S16, this means that since Z_* effectively traces the Fe abundance in stars, a combination of low Z_* and moderate Z_{neb} in high- z galaxies does not require the stellar O/H to differ from O/H in the gas—because O/Fe may be enhanced relative to $(\text{O/Fe})_\odot$ by up to a factor of ~ 5.5 (Nomoto et al. 2006).

In the case of the composite spectrum of 30 KBSS galaxies from S16, we demonstrated that the UV-optical nebular properties were consistent with $Z_{\text{neb}}/Z_\odot = 0.5$, while the shape of the rest-UV spectrum was globally best fit by population synthesis models with $Z_*/Z_\odot \approx 0.1$. Together these results imply $\text{O/Fe} \simeq 4\text{--}5(\text{O/Fe})_\odot$, consistent with the Nomoto et al. (2006) yields for low- Z_* core-collapse SNe. Since we are now interested in comparing the model predictions with observations of the ensemble of $z \sim 2.3$ KBSS-MOSFIRE galaxies, we consider two separate models with $Z_*/Z_\odot = 0.07$ (BPASSv2-z001) and $Z_*/Z_\odot = 0.28$ (BPASSv2-z004) in order to account for a range in the Fe content of massive stars in high- z galaxies. As we will show in Section 6.2.1, significantly higher values of Z_* ($\gtrsim 0.5 Z_\odot$) can be ruled out for the majority of $z \sim 2.3$ galaxies by comparison with their nebular spectra alone.

6.1. Ionization Parameter

When the input ionizing spectrum is fixed, the photoionization model predictions are restricted to a surface in line ratio space, with each point on the surface defined by a unique combination of U and Z_{neb} . The space occupied by the photoionization model surface can be compared with line ratio measurements from the full $z \sim 2.3$ KBSS-MOSFIRE sample to understand the allowed range in both parameters and also how they are correlated with one another across the galaxy population.

Inconveniently, the photoionization model surface “folds over” in many 2D line ratio spaces, requiring constraints from many individual line ratios to break the degeneracy between combinations of U and Z_{neb} that result in at least some of the same observed line ratios. Fortunately, O32 and Ne3O2 (see Table 3) are substantially more sensitive to changes in U than changes in Z_{neb} , and we use measurements of these line ratios to independently constrain the likely values of ionization parameter.

Figure 21 illustrates how the predicted value of the O32 index varies as a function of $\log(U)$, assuming $Z_*/Z_\odot = 0.07$ (red points) or $Z_*/Z_\odot = 0.28$ (blue squares); the nebular oxygen abundance is assumed to be $Z_{\text{neb}}/Z_\odot = 0.5$ in both cases. The 68% highest density interval (HDI, the narrowest range that includes 68% of the sample) for O32 in the KBSS-MOSFIRE sample is indicated by the vertical extent of the shaded region, with a median O32 = 0.24. Using the predictions from the models, the corresponding ranges in $\log(U)$ needed to reproduce the observed range in O32 are

$$\begin{aligned} \log(U)_{z001,68\%} &= [-3.14, -2.61] \\ \log(U)_{z004,68\%} &= [-3.06, -2.52]. \end{aligned}$$

Note that the inferences made assuming $Z_*/Z_\odot = 0.28$ are shifted toward higher $\log(U)$ by ~ 0.08 dex. This trend extends to higher Z_* as well, such that higher values of U are required

¹⁰ We discuss the effects of restricting the BPASSv2 IMF to a maximum of $100 M_\odot$ in S16, which do not impact any of the results of this paper.

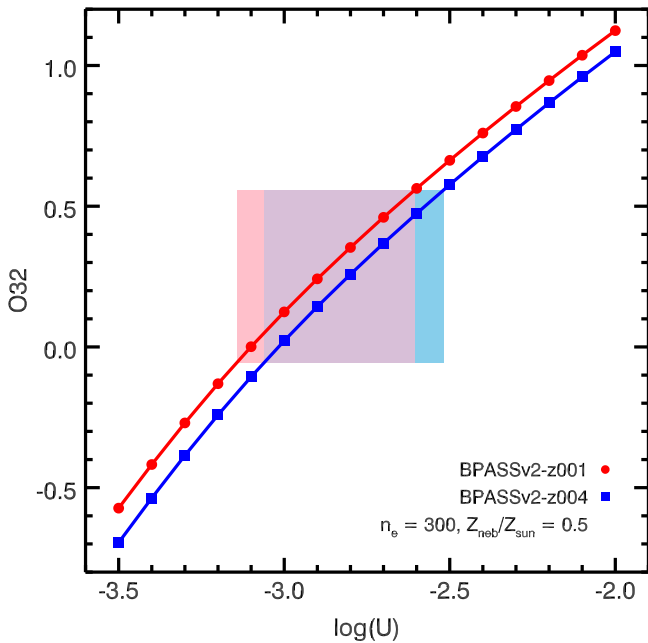


Figure 21. O32 as a function of $\log(U)$ for BPASSv2 models with $Z_*/Z_\odot = 0.07$ (red points) and $Z_*/Z_\odot = 0.28$ (blue squares). The metallicity of the gas is assumed to be $Z_{\text{neb}}/Z_\odot = 0.5$ in both cases. The vertical extent of the shaded region denotes the 68% HDI in O32 for the KBSS-MOSFIRE sample; the width of the shaded region shows the corresponding intervals in $\log(U)$ for the models (values provided in the text).

to produce the same value of O32 as Z_* increases. This trend—highlighting the trade-off between ionization parameter and hardness of the ionizing radiation field—is discussed more generally by Sanders et al. (2016).

The Ne3O2 index serves as a powerful cross-check on ionization parameters determined using O32, as it is significantly less affected by differential extinction due to dust, does not require any cross-band calibration, and provides an additional constraint on the shape of incident ionizing radiation. As with O32, however, the translation from Ne3O2 to U depends sensitively on the details of the photoionization model, particularly on the choice of the ionizing spectrum. In brief, because the ionization potential of Ne^+ (40.96 eV) is larger than that of O^+ (35.12 eV), which is the probe of high-ionization emission in the O32 index, the Ne3O2 index responds to changes in the shape of the EUV stellar spectrum at higher energies than O32. Thus Ne3O2 is predicted to increase relative to O32 with increasing hardness of the ionizing spectrum.

Figure 22 shows both indices, Ne3O2 and O32, for $z \sim 0$ SDSS galaxies (in grayscale, 90% contour in orange) and the $z \sim 2.3$ KBSS-MOSFIRE sample selected as outlined in Table 1 (green points with error bars). The linear fit to the data, accounting for errors in both line indices, is shown by the solid purple line, with the 1σ uncertainty in the fit parameters represented by the hatched purple region.

For comparison, the nebular line ratio predictions from the $Z_*/Z_\odot = 0.07$ (red points) and $Z_*/Z_\odot = 0.28$ (blue squares) models shown in Figure 21 are also included in Figure 22, with $\log(U)$ limited to the range identified using O32 measurements alone. The $Z_*/Z_\odot = 0.07$ model predicts slightly higher values of Ne3O2 at fixed O32 than the $Z_*/Z_\odot = 0.28$ model, but both agree well with the ridge-line of $z \sim 2.3$ galaxies.

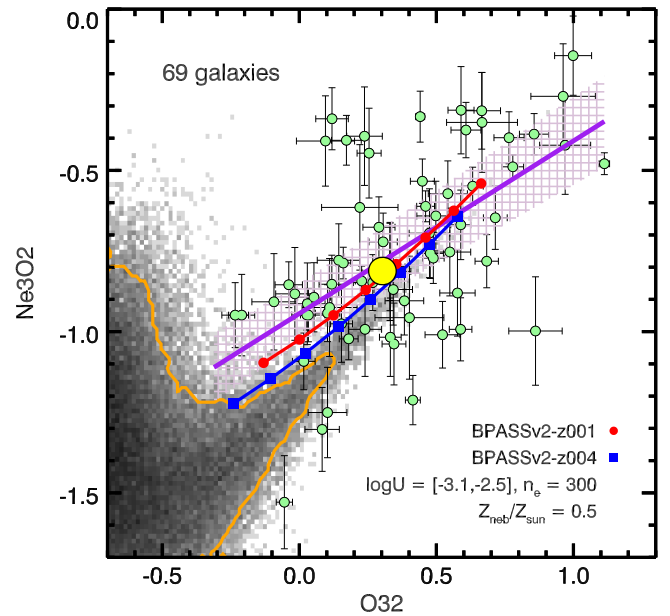


Figure 22. The distribution of Ne3O2 vs. O32 for KBSS-MOSFIRE (green points with error bars) and SDSS (in grayscale) galaxies, with the orange contour enclosing 90% of the $z \sim 0$ sample; the location of the S16 stack is identified by the large yellow point. The solid purple line shows the fit to the KBSS-MOSFIRE sample, with the 1σ errors in the fit parameters represented by the hatched purple region. The nebular line ratio predictions for BPASSv2 models with $Z_*/Z_\odot = 0.07$ (red points) and $Z_*/Z_\odot = 0.28$ (blue squares) are shown for $Z_{\text{neb}}/Z_\odot = 0.5$ and $\log(U) = [-3.1, -2.5]$, with the lowest values of $\log(U)$ corresponding to low O32 and Ne3O2.

Although we have thus far assumed a single gas-phase metallicity, the inferred range of $\log(U)$ is not particularly sensitive to Z_{neb} . Figure 23 shows the effect of changing Z_{neb} on the predicted line indices for three separate stellar metallicities: $Z_*/Z_\odot = 0.07$ (red), $Z_*/Z_\odot = 0.56$ (purple), or $Z_*/Z_\odot = 1.0$ (orange). For each value of $\log(U)$, the sequence in Z_{neb} is illustrated by a series of connected points, with increasing symbol size reflecting larger values of Z_{neb} ; grid points with $Z_{\text{neb}}/Z_\odot = 0.5$ are identified by darker-colored symbols. Regardless of Z_* , the differences in the predicted line indices are substantially larger for changes in U than for changes in Z_{neb} , particularly at low ionization parameters. At high U , the effect of decreasing Z_{neb} is more pronounced, but degenerate with changes in U .

However, the choice of Z_* does have a noticeable impact on the model predictions for Ne3O2 and O32. Figure 23 shows that increasing Z_*/Z_\odot from 0.07 to 0.56 decreases the predicted value of Ne3O2 by ~ 0.4 dex at every value of $\log(U)$; the corresponding decrease in O32 is ~ 0.3 dex. Although it is possible to reproduce separate values of Ne3O2 or O32 with other combinations of Z_* , Z_{neb} , and U , the model assuming $Z_*/Z_\odot = 0.07$ (red points) is best able to match the combinations of Ne3O2 and O32 observed in KBSS-MOSFIRE galaxies, represented by the gray shaded region in Figure 23.

6.2. Comparison with Other Nebular Diagnostics

6.2.1. The O32-R23 Diagram

Figure 24 compares predictions for O32 and R23 from the photoionization models with observations of the KBSS-MOSFIRE and SDSS galaxies; the sample of KBSS-MOSFIRE

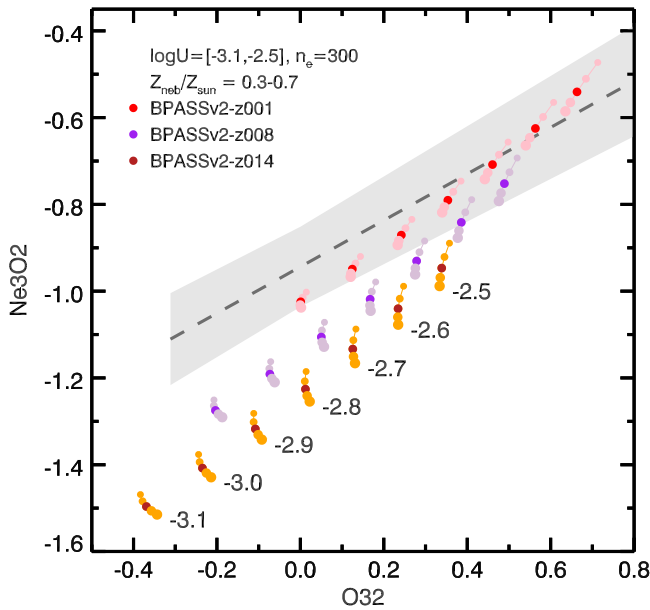


Figure 23. Photoionization model predictions for Ne3O2 and O32 for a range of Z_* and Z_{neb} . Each color reflects a different stellar metallicity: $Z_*/Z_\odot = 0.07$ (red), $Z_*/Z_\odot = 0.56$ (purple), and $Z_*/Z_\odot = 1.0$ (orange). The gas-phase metallicity sequence at each $\log(U)$ is represented by the connected points, with the increasing size of the symbol reflecting an increase in Z_{neb}/Z_\odot from 0.3–0.7; the grid points with $Z_{\text{neb}}/Z_\odot = 0.5$ are identified by darker-colored symbols. For comparison, the locus of $z \sim 2.3$ galaxies is represented by the gray line and shaded region, which is identical to the hatched region in Figure 22.

galaxies is identical to the sample introduced in Section 3.4 and is represented by the green points with error bars. The allowed range in ionization parameter has been set by the results from the previous section and matches the values shown in Figure 22, but we now consider a range in gas-phase metallicity: $Z_{\text{neb}}/Z_\odot = 0.1 - 1.0$.

The metallicity sequences for both models are shown by the series of connected points in Figure 24 and are nearly horizontal, with changes in Z_{neb} (reflected by the symbol size) resulting in motion to the left or right (in R23). Independently, changes in U move points vertically (in O32). Thus extending models with fixed Z_* to higher values of U and/or lower Z_{neb} cannot produce the high values of R23 at high O32 that are characteristic of both the $z \sim 2.3$ KBSS-MOSFIRE sample and the extreme tail of SDSS. Models with the lowest gas-phase metallicities (the smallest red points and blue squares) are among the most discrepant with respect to the data; only grid points with $Z_{\text{neb}}/Z_\odot \approx 0.3-0.9$ can match the line indices observed for the majority of galaxies, but the location of individual objects will be equally (or more) sensitive to changes in U and Z_* .

These results present severe challenges to using the combination of O32 and R23 as a metallicity determination method for objects in this region of parameter space. Because of the narrow high-ionization sequence at both $z \sim 0$ and $z \sim 2.3$ and the double-valued nature of the R23 index, galaxies with different Z_{neb} but similar values of U may exhibit similar values of R23 at fixed O32 and thus be spatially coincident in Figure 24. As discussed in Section 5.3, the difference in N/O between SDSS twins (identified in the O32-R23 diagram) and KBSS-MOSFIRE galaxies imply that $z \sim 2.3$ galaxies have 0.06 dex higher $12+\log(\text{O}/\text{H})$ than

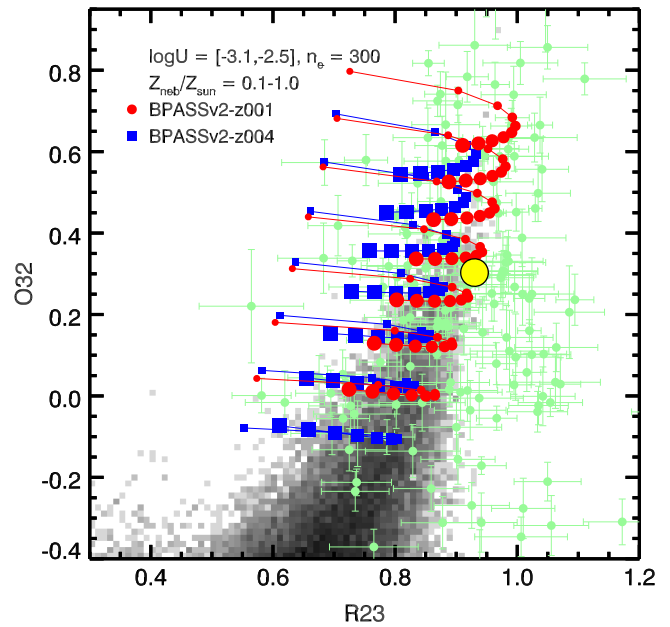


Figure 24. A comparison between the photoionization model predictions for O32 and R23 and the location of $z \sim 2.3$ KBSS-MOSFIRE and $z \sim 0$ SDSS galaxies, with the location of the S16 stack identified by the large yellow point. A range of ionization parameters and gas-phase metallicities are considered, with the Z_{neb} sequence at each value of U connected by a line; the increasing size of the points reflects increasing Z_{neb}/Z_\odot from 0.1 to 1.0. At fixed O32 and Z_{neb} , the only way to increase the maximum value of R23 is to change the shape of the ionizing radiation, here parameterized by Z_* .

$z \sim 0$ galaxies with the same ionizing spectral shape. Thus if a KBSS-MOSFIRE galaxy has $Z_{\text{neb}}/Z_\odot = 0.5$, then its $z \sim 0$ twin should have $Z_{\text{neb}}/Z_\odot = 0.44$, and the insensitivity of O32 and R23 to Z_{neb} (particularly near the turnaround in R23) will render them virtually indistinguishable in Figure 24. An apparent metallicity sequence in the O32-R23 plane could arise due to an anti-correlation between the ionization parameter and O/H, as proposed by Sanders et al. (2016), but the relationship between those parameters may not be redshift invariant and is sensitive to the shape of the incident ionizing radiation. Because the shape of the EUV radiation is regulated largely by the Fe content of massive stars (Z_*), it can differ greatly for galaxies with the same O/H (Z_{neb}) if they have different values of O/Fe.

The O32-R23 diagram serves as a much more sensitive diagnostic of the shape and normalization of the ionizing radiation fields in H II regions and galaxies, in part because it is so insensitive to Z_{neb} for objects with high values of both indices. Figure 25 compares the interquartile range of R23 for $z \sim 2.3$ KBSS-MOSFIRE galaxies with O32 ratios within 2σ of the median, and O32 = 0.10–0.40 (represented by the horizontal gray band) with R23 predictions from photoionization models spanning $Z_*/Z_\odot = 0.07-1.0$. The colored points represent the median R23 value for all model grid points ($Z_{\text{neb}}/Z_\odot = 0.1-1.0$ and $\log(U) = [-3.5, -2.0]$) with O32 = 0.10–0.40 at each Z_* ; the error bars show the minimum and maximum R23 values. For $Z_*/Z_\odot \gtrsim 0.5$, even the maximum value of R23 in this range of O32 is too low to match the majority of $z \sim 2.3$ galaxies, which suggests that the ionizing spectra in most KBSS-MOSFIRE galaxies are consistent with low- Z_* BPASSv2 models. It is important to note that the actual constraint imposed by the comparison of the data with the model predictions is on the *shape* of the stellar

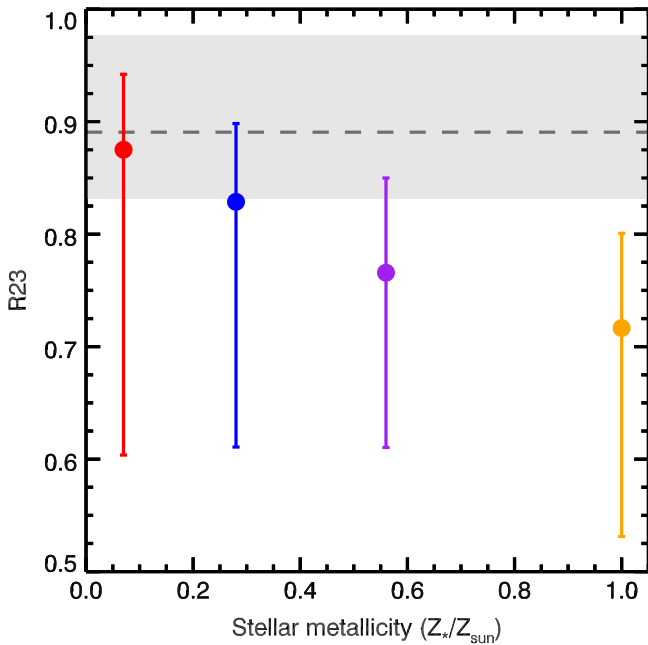


Figure 25. The range of predicted R23 indices from BPASSv2 models with a range of Z_* compared with the interquartile range observed in $z \sim 2.3$ KBSS-MOSFIRE galaxies with O32 ratios within 2σ of the median, $O32 = 0.10\text{--}0.40$ (horizontal gray band, with the median R23 shown by the dashed line). The colored points represent the median R23 value predicted for all combinations of Z_{neb} and U at fixed Z_* for grid points with equivalent O32 ratios; the error bars show the minimum and maximum R23 predicted for the same grid points. Notably, models assuming $Z_*/Z_\odot \gtrsim 0.5$ predict peak values of R23 that are too low to match the majority of $z \sim 2.3$ galaxies, suggesting high Z_* is not typical in this sample.

population EUV SED in the 1–4 Ryd range, and the implementation of low-metallicity binaries in BPASSv2 is simply one realistic way of achieving that spectral shape.

6.2.2. The BPT Diagrams

We now return to the BPT diagrams, using constraints from the rest-UV spectral analysis presented in S16 combined with the analysis presented earlier in this paper. To summarize, we adopt

$$\begin{aligned} n_e &= 300 \text{ cm}^{-3} \\ \log(U) &= [-3.1, -2.5] \\ Z_*/Z_\odot &= 0.07 - 0.28 \\ Z_{\text{neb}}/Z_\odot &= 0.3 - 0.9 \end{aligned}$$

as the optimal combination of parameters capable of reproducing the nebular properties of $z \sim 2.3$ KBSS-MOSFIRE galaxies.

The relation between N/O and O/H in the photoionization models is motivated by the agreement between the Pil12 sample and KBSS-MOSFIRE galaxies shown in Section 5.2. As shown in Figure 18, however, the apparent N/O–O/H relation for the KBSS-MOSFIRE sample would imply supersolar values of N/O at solar O/H, a feature common to many empirical relations for N/O–O/H. Evidence suggests that this discrepancy arises from the tendency of direct T_e -based abundances to underestimate the true nebular O/H, in part because the highest temperature regions of nebulae will contribute more to the total flux in collisionally excited lines than cooler regions. We discussed this topic in detail in Section

8.1.2 of S16, but we refer to one specific example from the literature here: Esteban et al. (2014) found that direct method oxygen abundances based on measurements of collisionally excited lines from the H II regions of nearby galaxies were 0.24 ± 0.02 dex lower than the oxygen abundances determined from measurements of nebular recombination lines. Recombination line methods are less temperature-sensitive and often agree better with stellar abundances when gas-phase and stellar abundances are measured for the same systems. Motivated by this significant difference, we introduce a $+0.23$ dex shift in $12 + \log(\text{O}/\text{H})$ to Equation (8), which forces the relation to produce $(\text{N}/\text{O})_\odot$ at $(\text{O}/\text{H})_\odot$. The final relation used in the photoionization models is then

$$\begin{aligned} \log(\text{N}/\text{O}) &= 1.68 \times \log(Z_{\text{neb}}/Z_\odot) - 0.86; Z_{\text{neb}}/Z_\odot > 0.4 \\ \log(\text{N}/\text{O}) &= -1.5; Z_{\text{neb}}/Z_\odot \leq 0.4. \end{aligned} \quad (9)$$

Figure 26 shows the range of line ratios observed in KBSS-MOSFIRE galaxies in the N2-BPT and S2-BPT planes compared with predictions from the photoionization models. The best-fit loci for the KBSS-MOSFIRE sample are represented by the dark green curves, with the KBSS-MOSFIRE sample plotted as light green points with error bars. The models are illustrated in a similar manner to Figure 24, where the metallicity sequence at each value of $\log(U)$ is connected by a line and the size of the point reflects the value of Z_{neb}/Z_\odot .

Foremost, we note that the model predictions agree well with the range of KBSS-MOSFIRE observations in both diagrams, as they have for the other combinations of line indices presented in this section. The ability of the BPASSv2 models to self-consistently reproduce many of the commonly used strong rest-optical emission line ratios across the $z \sim 2.3$ sample is encouraging. It also confirms that the radiation fields in the majority of high-redshift galaxies must at least resemble the spectra produced by stellar populations with $Z_*/Z_\odot = 0.07\text{--}0.28$ that include massive binaries.

In contrast to the locus of $z \sim 2.3$ galaxies in the O32-R23 diagram, which provides only weak constraints on the likely range of Z_{neb} , the left panel of Figure 26 shows that moderately high Z_{neb} is required to reproduce the high values of $\log([\text{N II}]/\text{H}\alpha)$ observed at fixed $\log([\text{O III}]/\text{H}\beta)$. However, despite exhibiting an offset relative to the locus of SDSS galaxies in the N2-BPT diagram, the photoionization model predictions for $Z_{\text{neb}}/Z_\odot \approx 0.6\text{--}0.9$ overlay the high- $[\text{O III}]/\text{H}\beta$ tail of SDSS in the S2-BPT diagram—as observed for the KBSS-MOSFIRE galaxies. The strong offset of $z \sim 2.3$ galaxies relative to SDSS in the N2-BPT diagram with little to no corresponding offset in the S2-BPT plane is actually a prediction of photoionization models that include hard ionizing radiation from relatively low- Z_* stars and relatively high- Z_{neb} gas.

We may also use observations of SDSS galaxies in the N2- and S2-BPT diagrams to constrain the combination of photoionization model parameters that would successfully describe $z \sim 0$ galaxies with the highest ratios of $[\text{O III}]/\text{H}\beta$, such as the SDSS twins introduced in Section 5.3. The location of the SDSS twins in the O32-R23 diagram (Figure 19) provides a compelling argument that the shape and normalization of their ionizing radiation fields (and thus Z_* and U) are similar to those observed in KBSS-MOSFIRE galaxies and that predictions from the same BPASSv2 models are appropriate. In the left panel of Figure 26, the SDSS twins are identified by open orange squares and most closely matched by models with

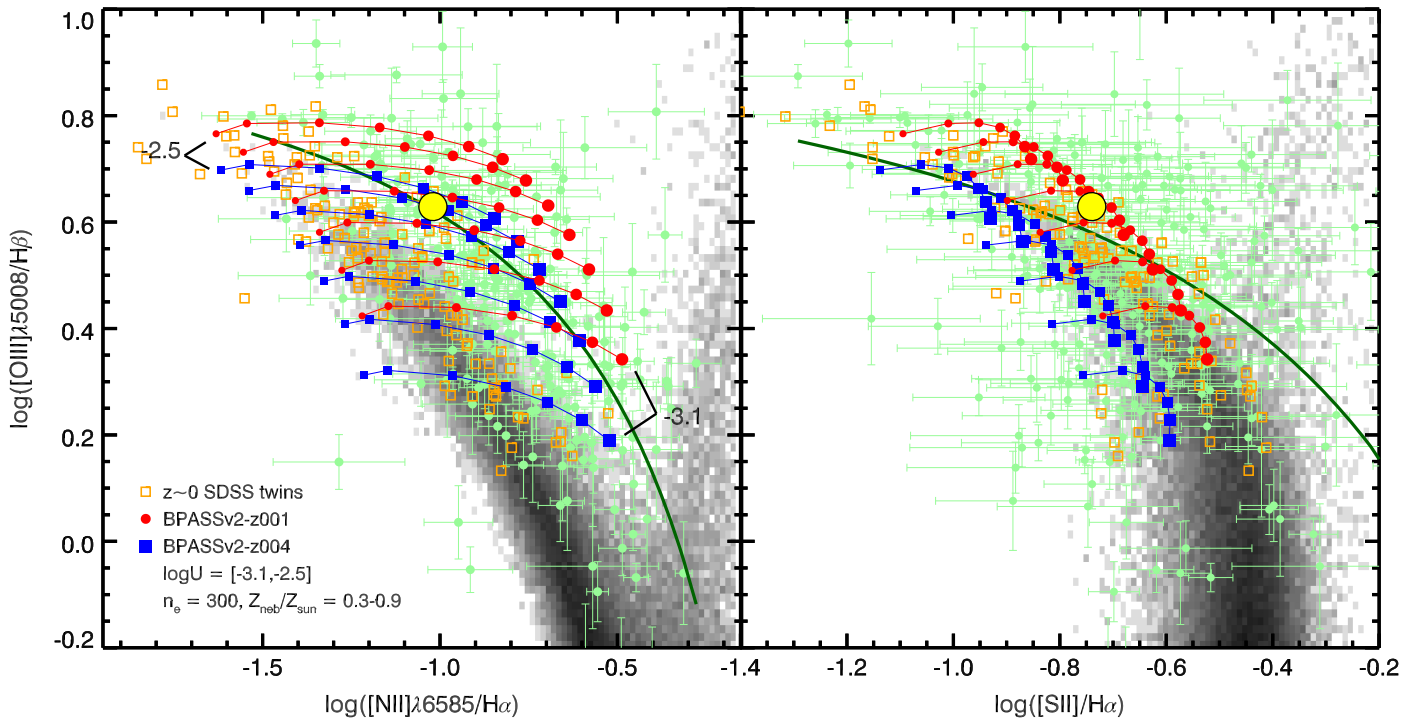


Figure 26. A comparison between the range of nebular emission line ratios predicted by the photoionization models described in the text and those observed in $z \sim 2.3$ KBSS-MOSFIRE galaxies (represented by the green points with error bars, with the ridge-line shown by the solid green curve and the location of the S16 stack identified by the large yellow point). The model predictions are presented in the same manner as Figure 24, with the Z_{neb} sequence at each value of U connected by a line; the size of the point reflects the level of gas-phase enrichment, which has been restricted to $Z_{\text{neb}}/Z_{\odot} = 0.3\text{--}0.9$. The model predictions agree well with the full range of observations in both panels and support the results from Section 5.3: $z \sim 2.3$ galaxies and SDSS twins (matched in O32 and R23, Figure 19) are consistent with having the same relatively hard ionizing spectra, but KBSS-MOSFIRE galaxies require higher Z_{neb} to explain their nebular line ratios. The most offset $z \sim 2.3$ galaxies in the N2-BPT are consistent with values of Z_{neb} that make them indistinguishable from the SDSS locus in the S2-BPT plane, meaning that an offset in $[\text{N II}]/\text{H}\alpha$ with no corresponding offset in $[\text{S II}]/\text{H}\alpha$ is a prediction of the models.

$Z_{\text{neb}}/Z_{\odot} \approx 0.3\text{--}0.5$; the same model parameters also provide good agreement with observations of the SDSS twins in the S2-BPT diagram. That SDSS galaxies matched in O32 and R23 appear to have lower Z_{neb} than KBSS-MOSFIRE galaxies (which require Z_{neb}/Z_{\odot} up to ≈ 0.9) is compatible with the significantly different distributions of N/O for the SDSS twins and KBSS-MOSFIRE galaxies (panel (c) in Figure 20) and the N/O–O/H relation from Equation (8).

6.3. O/H Constraints from Photoionization Models

The discussion in this section explicitly highlights the separate impact that gas chemistry (including both N/O and O/H) and the shape and normalization of the ionizing radiation (parameterized by Z_{*} and U) have on the nebular spectra of H II regions. Although the combination of O32 and R23 is relatively insensitive to gas-phase oxygen abundance in high-excitation nebulae (like those in $z \sim 2.3$ galaxies and in the SDSS twins), the O32-R23 diagram is especially powerful for constraining the shape of the EUV radiation field, because the line indices trace the ionization parameter and excitation almost independently.

Conversely, the location of galaxies in the N2-BPT diagram depends sensitively on almost every parameter of interest—gas-phase oxygen abundance, N/O, ionization parameter, and the shape of the ionizing radiation field—making it difficult to disentangle the contributions of each. Fortunately, surveys like KBSS-MOSFIRE allow us to leverage observations of $z \sim 2.3$ galaxies in a multidimensional nebular line ratio space to constrain these quantities for individual galaxies through

comparisons with photoionization models, without requiring a recalibration of the relationship between O/H and the strong-line indices. The utility of this method has already been demonstrated for composite spectra by S16, where the oxygen abundance could be measured directly using T_e , and independent constraints on the most likely input ionizing radiation field were available from comparisons between stellar population models and the rest-UV spectrum. The agreement between the BPASSv2 models and the extent of the full KBSS-MOSFIRE sample in multiple parameter spaces suggests that similar families of models may be applied directly to observations of individual galaxies, which is the focus of future work. Self-consistent measurements of O/H, N/O, and U for a large sample of $z \sim 2.3$ galaxies will allow us to directly investigate the N/O–O/H relation and the correlation between metallicity and U .

7. What Causes the $z \sim 2.3$ BPT Offset?

Returning to the question that has been the subject of much scientific debate over the last few years—“What causes the BPT offset?”—we are now better equipped to determine which mechanism or combination of mechanisms is likely to be primarily responsible, both for explaining the differences between samples of galaxies at $z \sim 0$ and $z \sim 2.3$ and between galaxies at the same redshift. We have already shown that the offset of $z \sim 2.3$ galaxies with respect to SDSS in the N2 BPT plane cannot be attributed only to selection and observational biases (Figures 12 and 14). In this section, we use the combined analysis of the rest-optical spectra of KBSS-MOSFIRE

galaxies to evaluate the relative importance of some of the most frequently proposed physical explanations.

Ubiquitous AGN activity. Like $z \sim 2$ galaxies from other surveys, the KBSS-MOSFIRE sample occupies a region in the N2-BPT diagram that is populated almost exclusively by AGN or composite galaxies at $z \sim 0$ (Figure 5). Additionally, the values of $\log([\text{O III}]/\text{H}\beta)$ observed in the $z \sim 2.3$ galaxies are ~ 0.8 dex higher than local star-forming galaxies at fixed M_* and thus similar to local AGN (Figure 7). However, there is no evidence of AGN activity in the rest-UV spectra of most KBSS-MOSFIRE galaxies with complementary LRIS observations (see S14); very high values of $\log([\text{N II}]/\text{H}\alpha)$ or large rest-optical line widths are also rare. In total, only 7/377 KBSS-MOSFIRE galaxies with measurements that place them on the N2-BPT diagram are identified as AGN or QSOs (Section 3.2). Although the supermassive black holes in these galaxies are almost certainly accreting gas, the resulting effect on the total nebular spectrum is subdominant with respect to ongoing star formation.

Higher electron density. In the local universe, n_e is correlated with the location of galaxies in the N2-BPT plane (Brinchmann et al. 2008; Liu et al. 2008; Yuan et al. 2010). Because the characteristic n_e observed in high-redshift galaxies is 10 times higher than galaxies at $z \sim 0$, with typical values of $\approx 200\text{--}300 \text{ cm}^{-3}$ at $z \sim 2.3$ (e.g., Steidel et al. 2014; Sanders et al. 2016), it is important to quantitatively assess whether this difference is sufficient to explain the observed N2-BPT offset. As shown in Figure 15, however, measurements of the density-sensitive $[\text{O II}]$ doublets for small- and large-offset KBSS-MOSFIRE galaxies (Figure 9) are nearly identical. Given that the inferred electron densities for both subsamples are consistent within errors, we conclude that a difference in n_e cannot account for the still significant offset between the small- and large-offset N2-BPT loci, and thus is unlikely to be the primary driver of the overall $z \sim 2.3$ offset.

Enhanced N/O at fixed O/H. Several authors have interpreted the strong offset of high- z galaxies in the N2-BPT plane (and lack of corresponding offset in the S2-BPT and O32-R23 diagrams) as evidence for larger N/O at fixed O/H (including Masters et al. 2014, 2016; Shapley et al. 2015; Cowie et al. 2016; Sanders et al. 2016), an explanation that naturally results in larger values of $\log([\text{N II}]/\text{H}\alpha)$ while leaving line ratios not including N unaffected. This enhancement, if it exists, should also be reflected in the correlation between N/O and other galaxy properties (such as M_*), particularly given the strong but evolving correlation between O/H and M_* observed at all redshifts.

We showed in Figure 17 that at fixed M_* , $z \sim 2.3$ KBSS-MOSFIRE galaxies exhibit values of $\log(\text{N/O})$ that are lower by an average of ~ 0.32 dex relative to SDSS galaxies. Galaxies at $z \sim 2.3$ also have lower $12+\log(\text{O/H})$ than SDSS galaxies by a comparable amount (Steidel et al. 2014; Wuyts et al. 2014; Sanders et al. 2015), suggesting that there is a relatively constant N/O–O/H relation for all galaxies. Additional evidence in support of this interpretation comes from the comparison of the composite UV-optical nebular spectrum from S16 with a sample of $z \sim 0$ H II regions from Pilyugin et al. (2012), with the $z \sim 2.3$ stack exhibiting N/O at fixed O/H consistent with the local relation.

KBSS-MOSFIRE galaxies do show 0.10 dex larger values of $\log(\text{N/O})$ with respect to SDSS galaxies matched in O32 and R23 (as described in Section 5.3), consistent with the results

reported by Shapley et al. (2015) for $z \sim 2$ MOSDEF galaxies, but we argue that samples matched in O32 and R23 are more likely to share ionizing radiation fields than gas-phase oxygen abundance. Assuming the N/O–O/H relation from Equation (8), this difference in N/O would accompany a 0.06 dex difference in $12+\log(\text{O/H})$, which would not be readily apparent from the locations of galaxies in the O32-R23 diagram (Figure 24). We note that even if the higher N/O measurements represent an enhancement at fixed O/H, this can account for $<55\%$ of the 0.37 dex horizontal displacement of the $z \sim 2.3$ locus with respect to the $z \sim 0$ locus in Figure 5. Thus, even if high- z galaxies were moderately N/O-enhanced, an additional mechanism (such as harder ionizing radiation fields) would still be required to explain the differences between $z \sim 2.3$ and $z \sim 0$.

Hard ionizing spectra of Fe-poor massive binaries. The analysis in Section 6 uses predictions from a subset of the photoionization models we considered in S16 to constrain the likely combination of U and Z_{neb} in the ensemble of KBSS-MOSFIRE observations. Adopting two BPASSv2 models with $Z_*/Z_\odot = 0.07$ and $Z_*/Z_\odot = 0.28$, we find that the line ratios observed in $z \sim 2.3$ galaxies are consistent with $\log(U) = [-3.1, -2.5]$ and $Z_{\text{neb}}/Z_\odot \approx 0.3\text{--}0.9$. We are not able to place direct constraints on O/Fe in individual galaxies in the manner of S16, but we note that the upper range in Z_{neb}/Z_* obtained from comparisons with the full KBSS-MOSFIRE sample broadly agrees with the O/Fe reported for the composite spectra ($\approx 4\text{--}5(\text{O/Fe})_\odot$).

We argue, as we did in S14 and S16, that the primary cause of the differences observed between typical galaxies at high-redshift and galaxies in the local universe is the degree of nebular excitation, with $z \sim 2.3$ galaxies exhibiting significantly higher values of $[\text{O III}]/\text{H}\beta$ and R23 relative to the majority of $z \sim 0$ galaxies. These line ratios—especially the high values of R23 observed at high O32 in KBSS-MOSFIRE galaxies—can be explained by hard ionizing radiation fields, such as those produced by Fe-poor stellar populations that include massive binaries. Yet, when compared with SDSS galaxies with similar nebular excitation (like the SDSS twins from Section 5.3), KBSS-MOSFIRE galaxies are still substantially offset to higher $\log([\text{N II}]/\text{H}\alpha)$ at fixed $\log([\text{O III}]/\text{H}\beta)$ due to larger values of N/O (and likely O/H). Thus $z \sim 2.3$ galaxies must contain harder ionizing radiation fields at fixed gas-phase N/O and O/H to explain the N2-BPT offset relative to the locus of typical $z \sim 0$ galaxies.

7.1. Implications for Local Analogs

These results are a natural consequence of systematic differences in star formation history between high-redshift star-forming galaxies and galaxies occupying the low-redshift locus. As we reasoned in S16, the ISM in galaxies with roughly constant SFR and stellar population ages $\lesssim 1$ Gyr will reflect enrichment primarily from core-collapse SNe, with the resulting super-solar O/Fe abundances responsible for harder ionizing spectra (from Fe-poor stars) at a given O/H compared to galaxies with lower O/Fe. If the characteristic star formation histories of galaxies were SFR increasing with time (as might be more common at high redshift; Reddy et al. 2012; Steidel et al. 2016), high values of O/Fe could easily be maintained for longer than 1 Gyr. This is possible because, to first order, the enrichment rate of O is proportional to the current SFR, whereas the rate of enrichment of Fe (which comes primarily

from Type Ia SNe) is proportional to the SFR 1 Gyr earlier. Thus, given typical inferred ages of a few hundred Myr (Reddy et al. 2012), most $z \sim 2.3$ galaxies should be forming stars that are relatively α -enhanced (and O-enhanced), consistent with core-collapse SNe yields.

sSFR serves as a crude but easily measured probe of the overall star formation histories of galaxies. By definition, young stars make up a larger fraction of the stellar populations in galaxies with high sSFRs, and $1/\text{sSFR}$ is roughly equivalent to the age of the stellar population (assuming a constant SFR). Thus galaxies with $\text{sSFR} > 1 \text{ Gyr}^{-1}$ will have a substantial fraction of stars that formed from gas enriched almost entirely by Type II SNe. The median sSFR for the KBSS-MOSFIRE sample is 2.4 Gyr^{-1} , corresponding to a timescale of ~ 400 Myr, substantially less than the 1 Gyr timescale for the onset of Type Ia SNe; moreover, as we showed in Section 4.2, nearly 60% of KBSS-MOSFIRE galaxies have $\text{sSFR} > 2 \text{ Gyr}^{-1}$, corresponding to timescales < 500 Myr, with only $\sim 20\%$ having $\text{sSFR} < 1 \text{ Gyr}^{-1}$. In contrast, only $\sim 1\%$ of SDSS galaxies have $\text{sSFR} > 2 \text{ Gyr}^{-1}$, and such galaxies also have ~ 10 times smaller M_* compared with high-sSFR KBSS-MOSFIRE galaxies. For the majority of SDSS galaxies, $\text{sSFR} \sim 0.1 \text{ Gyr}^{-1}$; at these low sSFRs, the youngest stars represent a small contribution to the overall M_* , and their O/Fe abundances will closely reflect the end state of the galaxy’s chemical evolution.

It is clear that sSFR can be used to identify galaxies whose nebular properties are similar in some ways to typical galaxies at $z \sim 2.3$. However, the KBSS-MOSFIRE galaxies that are *most* offset from the SDSS star-forming sequence in the N2-BPT diagram represent an interesting population without exact analogs in the local universe: galaxies at $z \sim 0$ with similar ionizing spectra are ~ 10 times less massive than typical $z \sim 2.3$ galaxies and have significantly lower N/O and O/H, but $z \sim 0$ galaxies with similar M_* or gas-phase metallicity will have substantially softer ionizing radiation fields. The absence of a suitable comparison sample—with both high levels of nebular excitation (high [O III]/H β and R23) and high gas-phase metallicity—limits the utility of $z \sim 0$ analogs for studying the conditions in $z \sim 2.3$ systems significantly offset in the N2-BPT plane. Specifically, this raises concerns about using extreme $z \sim 0$ galaxies (like the SDSS twins) to construct an empirical strong-line metallicity calibration intended to be used at $z \gtrsim 2$. Any study using calibrations based on nebular line ratios that are sensitive to both gas-phase chemistry and the shape and normalization of the ionizing radiation field must take care to understand the impact of differences between the calibration and test samples.

8. Summary

We have presented a detailed analysis of the rest-optical (3600–7000 Å) spectra of $\sim 380 z \simeq 2\text{--}3$ star-forming galaxies drawn from the MOSFIRE component of the KBSS. Combining multiwavelength photometric observations and SED fitting with robust measurements of many of the commonly used strong nebular emission lines, we have shown the following.

1. KBSS-MOSFIRE galaxies at $z \sim 2.3$ exhibit a clear offset in the N2-BPT diagram relative to typical galaxies in the local universe, represented by SDSS (Figure 5). If one assumes the difference is along only one axis, the

magnitude of this offset is $\Delta \log([\text{N II}]/\text{H}\alpha) = 0.37$ dex or $\Delta \log([\text{O III}]/\text{H}\beta) = 0.26$ dex.

2. The same high- z galaxies have nebular properties consistent with the high-excitation tail of the $z \sim 0$ galaxy distribution in the S2-BPT (Figure 6) and O32-R23 (Figure 8) diagnostic diagrams.
3. The offset of $z \sim 2.3$ galaxies relative to the $z \sim 0$ N2-BPT locus is inversely correlated with M_* and positively correlated with sSFR. Likewise, sSFR is also strongly correlated with the degree of excitation (as probed by [O III]/H β and R23) for all galaxies (Figure 11).
4. Many of the most offset $z \sim 2.3$ KBSS-MOSFIRE galaxies have blue optical-NIR colors ($\mathcal{R} - K_s \leq 1$), high sSFRs ($\sim 7 \text{ Gyr}^{-1}$), and are best-fit by young (50 Myr) stellar population ages, assuming constant or increasing star formation histories (Figures 11, 12, and 13).
5. KBSS-MOSFIRE galaxies at $z \sim 2.3$ have 0.10 dex higher N/O than SDSS galaxies matched in O32 and R23 (panel (c) in Figure 20). If galaxies at all redshifts exhibit the same N/O–O/H relation (as we argue in Section 5.2), a 0.10 dex increase in $\log(\text{N/O})$ corresponds to a 0.06 dex increase in $12+\log(\text{O/H})$. Such a small change in O/H would have only a minor effect on the observed locations of galaxies in the O32-R23 and S2-BPT diagrams.
6. Observations of most $z \sim 2.3$ KBSS-MOSFIRE galaxies are consistent with photoionization models that use a binary population synthesis model (BPASSv2) with stellar metallicity $Z_*/Z_\odot = 0.07\text{--}0.28$ (Figure 25), gas-phase metallicity $Z_{\text{neb}}/Z_\odot \approx 0.3\text{--}0.9$, and ionization parameter $\log(U) = [-3.1, -2.5]$ (Figure 26). These models reproduce the large observed shift with respect to local star-forming galaxies in the N2-BPT diagram, but result in no appreciable offset between the predicted line ratios for $z \sim 2.3$ galaxies and the local sequence in the S2-BPT plane; thus this apparent discrepancy can be explained without needing to invoke elevated N/O at fixed O/H.

From these results, we conclude that the principal cause of the “BPT offset” is an increase in the hardness of the ionizing radiation at fixed N/O and O/H, consistent with the EUV spectra produced by Fe-poor stellar populations that include massive binaries.

We are grateful to the referee for the thoughtful and constructive feedback provided during the review process. We also thank the organizers and attendees of the Carnegie Symposium in honor of Leonard Searle, “Understanding Nebular Emission in High-redshift Galaxies,” held at the Carnegie Observatories in Pasadena, for many interesting conversations that contributed to the work presented here. This work has been supported in part by a US National Science Foundation (NSF) Graduate Research Fellowship (ALS), by the NSF through grants AST-0908805 and AST-1313472 (CCS, ALS, RFT, GCR), and by an Alfred P. Sloan Research Fellowship (NAR). Finally, the authors wish to recognize and acknowledge the significant cultural role and reverence that the summit of Maunakea has within the indigenous Hawaiian community. We are privileged to have the opportunity to conduct observations from this mountain.

References

- Adelberger, K. L., Steidel, C. C., Shapley, A. E., et al. 2004, *ApJ*, 607, 226
- Aihara, H., Allende Prieto, C., An, D., et al. 2011, *ApJS*, 193, 29
- Andrews, B. H., & Martini, P. 2013, *ApJ*, 765, 140
- Asplund, M., Grevesse, N., Sauval, A. J., & Scott, P. 2009, *ARA&A*, 47, 481
- Baldwin, J. A., Phillips, M. M., & Terlevich, R. 1981, *PASP*, 93, 5
- Brinchmann, J., Pettini, M., & Charlot, S. 2008, *MNRAS*, 385, 769
- Bruzual, G., & Charlot, S. 2003, *MNRAS*, 344, 1000
- Calzetti, D., Armus, L., Bohlin, R. C., et al. 2000, *ApJ*, 533, 682
- Campbell, A., Terlevich, R., & Melnick, J. 1986, *MNRAS*, 223, 811
- Cardelli, J. A., Clayton, G. C., & Mathis, J. S. 1989, *ApJ*, 345, 245
- Chabrier, G. 2003, *PASP*, 115, 763
- Coil, A. L., Aird, J., Reddy, N., et al. 2015, *ApJ*, 801, 35
- Cowie, L. L., Barger, A. J., & Songaila, A. 2016, *ApJ*, 817, 57
- Diaz, A. I., & Tosi, M. 1986, *A&A*, 158, 60
- Dickey, C. M., van Dokkum, P. G., Oesch, P. A., et al. 2016, *ApJL*, 828, L11
- Erb, D. K., Shapley, A. E., Pettini, M., et al. 2006a, *ApJ*, 644, 813
- Erb, D. K., Steidel, C. C., Shapley, A. E., et al. 2006b, *ApJ*, 646, 107
- Esteban, C., García-Rojas, J., Carigi, L., et al. 2014, *MNRAS*, 443, 624
- Ferland, G. J., Porter, R. L., van Hoof, P. A. M., et al. 2013, *RMxAA*, 49, 137
- Garnett, D. R. 1992, *AJ*, 103, 1330
- Hainline, K. N., Shapley, A. E., Greene, J. E., & Steidel, C. C. 2011, *ApJ*, 733, 31
- Hopkins, A. M., & Beacom, J. F. 2006, *ApJ*, 651, 142
- Juneau, S., Bournaud, F., Charlot, S., et al. 2014, *ApJ*, 788, 88
- Juneau, S., Dickinson, M., Alexander, D. M., & Salim, S. 2011, *ApJ*, 736, 104
- Kashino, D., Silverman, J. D., Sanders, D., et al. 2016, arXiv:1604.06802
- Kauffmann, G., Heckman, T. M., Tremonti, C., et al. 2003, *MNRAS*, 346, 1055
- Kennicutt, R. C., Jr. 1998, *ARA&A*, 36, 189
- Kewley, L. J., & Dopita, M. A. 2002, *ApJS*, 142, 35
- Kewley, L. J., Dopita, M. A., Leitherer, C., et al. 2013, *ApJ*, 774, 100
- Kewley, L. J., Dopita, M. A., Sutherland, R. S., Heisler, C. A., & Trevena, J. 2001, *ApJ*, 556, 121
- Kisielius, R., Storey, P. J., Ferland, G. J., & Keenan, F. P. 2009, *MNRAS*, 397, 903
- Köppen, J., & Hensler, G. 2005, *A&A*, 434, 531
- Kriek, M., Shapley, A. E., Reddy, N. A., et al. 2015, *ApJS*, 218, 15
- Law, D. R., Steidel, C. C., Shapley, A. E., et al. 2012, *ApJ*, 745, 85
- Lehnert, M. D., Nesvadba, N. P. H., Le Tiran, L., et al. 2009, *ApJ*, 699, 1660
- Liu, X., Shapley, A. E., Coil, A. L., Brinchmann, J., & Ma, C.-P. 2008, *ApJ*, 678, 758
- Madau, P., & Dickinson, M. 2014, *ARA&A*, 52, 415
- Madau, P., Ferguson, H. C., Dickinson, M. E., et al. 1996, *MNRAS*, 283, 1388
- Maiolino, R., Nagao, T., Grazian, A., et al. 2008, *A&A*, 488, 463
- Markwardt, C. B. 2009, in ASP Conf. Ser. 411, *Astronomical Data Analysis Software and Systems XVIII*, ed. D. A. Bohlender, D. Durand, & P. Dowler (San Francisco, CA: ASP), 251
- Masters, D., Faisst, A., & Capak, P. 2016, *ApJ*, 828, 18
- Masters, D., McCarthy, P., Siana, B., et al. 2014, *ApJ*, 785, 153
- McGaugh, S. S. 1991, *ApJ*, 380, 140
- McLean, I. S., Steidel, C. C., Epps, H. W., et al. 2012, *Proc. SPIE*, 8446, 84460J
- Mendoza, C., & Bautista, M. A. 2014, *ApJ*, 785, 91
- Nomoto, K., Tominaga, N., Umeda, H., Kobayashi, C., & Maeda, K. 2006, *NuPhA*, 777, 424
- Oke, J. B., Cohen, J. G., Carr, M., et al. 1995, *PASP*, 107, 375
- Osterbrock, D. E. 1989, *Astrophysics of Gaseous Nebulae and Active Galactic Nuclei* (Sausalito, CA: Univ. Science Books)
- Pagel, B. E. J., Edmunds, M. G., Blackwell, D. E., Chun, M. S., & Smith, G. 1979, *MNRAS*, 189, 95
- Penston, M. V., Robinson, A., Alloin, D., et al. 1990, *A&A*, 236, 53
- Pérez-Montero, E., & Contini, T. 2009, *MNRAS*, 398, 949
- Persson, S. E., Murphy, D. C., Smee, S., et al. 2013, *PASP*, 125, 654
- Pettini, M., & Pagel, B. E. J. 2004, *MNRAS*, 348, L59
- Pilyugin, L. S., Grebel, E. K., & Mattsson, L. 2012, *MNRAS*, 424, 2316
- Pilyugin, L. S., Vílchez, J. M., & Thuan, T. X. 2010, *ApJ*, 720, 1738
- Reddy, N. A., Pettini, M., Steidel, C. C., et al. 2012, *ApJ*, 754, 25
- Reddy, N. A., Steidel, C. C., Pettini, M., et al. 2008, *ApJS*, 175, 48
- Richards, G. T., Strauss, M. A., Fan, X., et al. 2006, *AJ*, 131, 2766
- Rudie, G. C., Steidel, C. C., Trainor, R. F., et al. 2012, *ApJ*, 750, 67
- Sanders, R. L., Shapley, A. E., Kriek, M., et al. 2015, *ApJ*, 799, 138
- Sanders, R. L., Shapley, A. E., Kriek, M., et al. 2016, *ApJ*, 816, 23
- Shapley, A. E., Reddy, N. A., Kriek, M., et al. 2015, *ApJ*, 801, 88
- Shapley, A. E., Steidel, C. C., Erb, D. K., et al. 2005, *ApJ*, 626, 698
- Sharples, R., Bender, R., Agudo Berbel, A., et al. 2013, *Msngr*, 151, 21
- Shivaei, I., Kriek, M., Reddy, N. A., et al. 2016, *ApJL*, 820, L23
- Stanway, E. R., Eldridge, J. J., & Becker, G. D. 2016, *MNRAS*, 456, 485
- Steidel, C. C., Rudie, G. C., Strom, A. L., et al. 2014, *ApJ*, 795, 165
- Steidel, C. C., Shapley, A. E., Pettini, M., et al. 2004, *ApJ*, 604, 534
- Steidel, C. C., Strom, A. L., Pettini, M., et al. 2016, *ApJ*, 826, 159
- Tacconi, L. J., Neri, R., Genzel, R., et al. 2013, *ApJ*, 768, 74
- Tayal, S. S., & Zatsarinny, O. 2010, *ApJS*, 188, 32
- van Zee, L., Salzer, J. J., & Haynes, M. P. 1998, *ApJL*, 497, L1
- Veilleux, S., & Osterbrock, D. E. 1987, *ApJS*, 63, 295
- Williams, M. J., Bureau, M., & Cappellari, M. 2010, *MNRAS*, 409, 1330
- Wisnioski, E., Förster Schreiber, N. M., Wuyts, S., et al. 2015, *ApJ*, 799, 209
- Wuyts, E., Kurk, J., Förster Schreiber, N. M., et al. 2014, *ApJL*, 789, L40
- York, D. G., Adelman, J., Anderson, J. E., Jr., et al. 2000, *AJ*, 120, 1579
- Yuan, T.-T., Kewley, L. J., & Sanders, D. B. 2010, *ApJ*, 709, 884